







## The Regulated NiCu Cycles with the new $^{57}\text{Cu}(p,\gamma)^{58}\text{Zn}$ reaction rate and the Influence on Type-I X-Ray Bursts: GS 1826–24 Clocked Burster

YI HUA LAM <sup>1,2</sup> NING LU <sup>1,2,3</sup> ALEXANDER HEGER <sup>4,5,6,7</sup> ADAM MICHAEL JACOBS <sup>7,8</sup> NADEZDA A. SMIRNOVA <sup>9</sup>  
TERESA KURTUKIAN NIETO,<sup>9</sup> ZAC JOHNSTON <sup>7,8</sup> AND SHIGERU KUBONO<sup>10,11</sup>

<sup>1</sup>CAS Key Laboratory of High Precision Nuclear Spectroscopy, Institute of Modern Physics,  
Chinese Academy of Sciences, Lanzhou 730000, People’s Republic of China

<sup>2</sup>School of Nuclear Science and Technology, University of Chinese Academy of Sciences, Beijing 100049, People’s Republic of China

<sup>3</sup>School of Nuclear Science and Technology, Lanzhou University, Lanzhou 730000, People’s Republic of China

<sup>4</sup>School of Physics and Astronomy, Monash University, Victoria 3800, Australia

<sup>5</sup>OzGrav-Monash – Monash Centre for Astrophysics, School of Physics and Astronomy, Monash University, VIC 3800, Australia

<sup>6</sup>Center of Excellence for Astrophysics in Three Dimensions (ASTRO-3D), Australia

<sup>7</sup>The Joint Institute for Nuclear Astrophysics, Michigan State University, East Lansing, MI 48824, USA

<sup>8</sup>Department of Physics and Astronomy, Michigan State University, East Lansing, MI 48824, USA

<sup>9</sup>CENBG, CNRS/IN2P3 and University of Bordeaux, Chemin du Solarium, 33175 Gradignan cedex, France

<sup>10</sup>RIKEN Nishina Center, 2-1 Hirosawa, Wako, Saitama 351-0198, Japan

<sup>11</sup>Center for Nuclear Study, University of Tokyo, 2-1 Hirosawa, Wako, Saitama 351-0198, Japan

(Received July 23, 2021)

Submitted to *Astrophys. J.*

### ABSTRACT

During the X-ray bursts of GS 1826–24, “clocked burster”, the nuclear reaction flow that surges through the rapid-proton capture process path has to pass through the NiCu cycles before reaching the ZnGa cycles that moderate the further extent of hydrogen burning in the region above germanium and selenium isotopes. The  $^{57}\text{Cu}(p,\gamma)^{58}\text{Zn}$  reaction located in the NiCu cycles plays an important role in influencing the burst light curves as found by [Cyburt et al. \(2016\)](#). We deduce the  $^{57}\text{Cu}(p,\gamma)^{58}\text{Zn}$  reaction rate based on the experimentally determined important nuclear structure information, isobaric-multiplet-mass equation, and large-scale shell model calculations. With the isobaric-multiplet-mass equation, we propose a possible order of  $1_1^+$  and  $2_3^+$  dominant resonance states that the  $2_3^+$  resonance state is higher than the  $1_1^+$  state, and estimate the resonance energy of  $1_2^+$  contributing resonance state. The new rate is up to a factor of five lower than the [Forstner et al. \(2001\)](#) rate recommended by JINA REACLIB v2.2. Using the one-dimensional implicit hydrodynamic code, KEPLER, to model the thermonuclear X-ray bursts of GS 1826–24 clocked burster, we find that the new  $^{57}\text{Cu}(p,\gamma)^{58}\text{Zn}$  reaction redistributes the reaction flow in the NiCu cycles and reduces the production of  $^{58}\text{Zn}$ , whereas the  $^{59}\text{Cu}(p,\alpha)^{56}\text{Ni}$  and  $^{59}\text{Cu}(p,\gamma)^{60}\text{Zn}$  reactions suppress the influence of the  $^{57}\text{Cu}(p,\gamma)^{58}\text{Zn}$  reaction and strongly diminish the impact of nuclear reaction flow that by-passes the important  $^{56}\text{Ni}$  waiting point induced by the  $^{55}\text{Ni}(p,\gamma)^{56}\text{Cu}$  reaction on burst light curve. The influence of the newly deduced  $^{56}\text{Ni}(p,\gamma)^{57}\text{Cu}$  is also discussed.

**Keywords:** nuclear reactions, nucleosynthesis, abundances — stars: neutron — X-rays: bursts

### 1. INTRODUCTION

Thermonuclear (Type I) X-ray bursts (XRBs) originate in the high density-temperature degenerate envelope of a neutron star in a close low-mass X-ray binary during thermonuclear runaways ([Woosley & Taam 1976](#); [Joss 1977](#)). The en-

velope consists of stellar material accreted from the low-mass companion star. Every episode of XRBs encapsulates abundant information of the hydrodynamics and thermal states of the evolution of the degenerate envelope ([Woosley et al. 2004](#)), the structure of the accreting neutron star ([Steiner et al. 2010](#)), the rapid-proton capture (rp-) process path of synthesized nuclei ([Van Wormer et al. 1994](#); [Schatz et al. 1998](#)), and the burst ashes that become compositional inertia for the succeeding bursts before sinking into the neutron-star crust ([Keek & Heger 2011](#); [Meisel et al. 2018](#)).

XRBs are driven by the triple- $\alpha$  reaction (Joss 1978),  $\alpha p$ -process (Woosley & Weaver 1984), rp-process (Wallace & Woosley 1981; Wiescher et al. 1987), and are constrained by  $\beta$ -decay and the proton dripline. After breaking out from the hot CNO cycle, the nuclear reaction flows enter the  $sd$ -shell nuclei region via  $\alpha p$ -processes, also this is the region of which the  $\alpha p$ -processes are dominant. Then, the reaction flows continue to the  $pf$ -shell nuclei region with first going through a few important cycles at the light  $pf$ -shell nuclei, e.g., the CaSc cycle, and then reach the medium  $pf$ -shell nuclei of which the NiCu and ZnGa cycles reside (Van Wormer et al. 1994). After breaking out from the ZnGa cycles and the GeAs cycle, which may transiently and weakly exist, and passing through Ge and Se isotopes, the reaction flows surge through the heavier proton-rich nuclei of where rp-processes actively burn the remaining hydrogen accreted from the companion star; and eventually the reaction flows stop at the SnSbTe cycles (Schatz et al. 2001). This rp-process path is indicated in the pioneering GS 1826–24 clocked burster model (Woosley et al. 2004; Heger et al. 2007).

The  $^{57}\text{Cu}(p,\gamma)^{58}\text{Zn}$  reaction that draws material from the  $^{56}\text{Ni}$  waiting point via the  $^{56}\text{Ni}(p,\gamma)^{57}\text{Cu}$  branch is located in the NiCu I cycle (Fig. 1). The influence of this reaction on XRB light curve and on burst-ash abundances was studied by Cyburt et al. (2016), and they concluded that the  $^{57}\text{Cu}(p,\gamma)^{58}\text{Zn}$  reaction is the fifth influential  $(p,\gamma)$  reaction that affects the light curve of GS 1826–24 clocked burster (Makino et al. 1988; Tanaka et al. 1989; Ubertaini et al. 1999). Forstner et al. (2001) constructed the  $^{57}\text{Cu}(p,\gamma)^{58}\text{Zn}$  reaction rate based on shell-model calculation and predicted the properties of important resonances. Later, Langer et al. (2014) experimentally confirmed some low-lying energy levels of  $^{58}\text{Zn}$ , which are dominant resonances contributing to the  $^{57}\text{Cu}(p,\gamma)^{58}\text{Zn}$  reaction rate at temperature range  $0.3 \lesssim T(\text{GK}) \lesssim 2.0$ . With the high precision measurement of these energy levels, Langer et al. largely reduced the rate uncertainty up to 3 orders of magnitude compared to Forstner et al. reaction rate. Nevertheless, the order of  $1_1^+$  and  $2_3^+$  dominating resonance states was unconfirmed, and the  $1_2^+$  resonance state, which is one of the dominant resonances at XRB temperature range,  $0.7 \lesssim T(\text{GK}) \lesssim 2$ , was not detected in their experiment.

The  $^{55}\text{Ni}(p,\gamma)^{56}\text{Cu}$  reaction rate was recently determined by Valverde et al. (2019) and Ma et al. (2019) with the highly-precisely measured  $^{56}\text{Cu}$  mass (Valverde et al. 2018) and the precisely measured excited states of  $^{56}\text{Cu}$  (Ong et al. 2017). In fact, Ma et al. (2019) found that the  $^{55}\text{Ni}(p,\gamma)^{56}\text{Cu}$  reaction rate was up to one order of magnitude underestimated by Valverde et al. (2018) due to the incorrect penetrability scaling factor, causing a set of wrongly determined burst-ash abundances of nuclei  $A = 55 - 60$ . Figure 2 presents the comparison of the  $^{55}\text{Ni}(p,\gamma)^{56}\text{Cu}$  reaction rates deduced by Valverde et al. (2019), Ma et al. (2019), and Fisker et al. (2001). The reaction rate was then corrected by Valverde et al. (2019) and used in their updated one-zone XRB model indicating that the reaction flow by-passing the important  $^{56}\text{Ni}$  waiting point could be established. Based on the updated

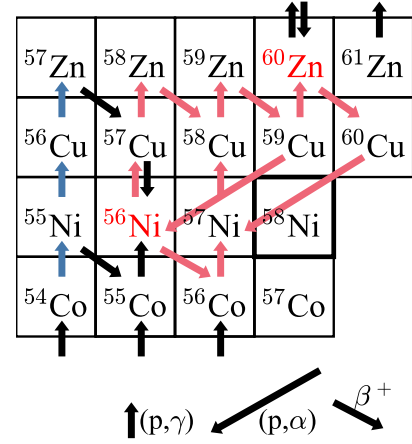


**Figure 1.** The rp-process path passing through the NiCu cycles. Stable nuclei are represented by thick black squares, and waiting points are shown in red texts. The NiCu cycles are displayed as red arrows. The NiCu I cycle consists of  $^{56}\text{Ni}(p,\gamma)^{57}\text{Cu}(p,\gamma)^{58}\text{Zn}(\beta^+\nu)^{58}\text{Cu}(p,\gamma)^{59}\text{Zn}(\beta^+\nu)^{59}\text{Cu}(p,\alpha)^{56}\text{Ni}$  reactions, and the NiCu II cycle is a series of  $^{57}\text{Ni}(p,\gamma)^{58}\text{Cu}(p,\gamma)^{59}\text{Zn}(\beta^+\nu)^{59}\text{Cu}(p,\gamma)^{60}\text{Zn}(\beta^+\nu)^{60}\text{Cu}(p,\alpha)^{57}\text{Ni}$  reactions (Van Wormer et al. 1994). The other sub-NiCu II cycle,  $^{56}\text{Ni}(\beta^+\nu)^{56}\text{Co}(p,\gamma)^{57}\text{Ni}(p,\gamma)^{58}\text{Cu}(p,\gamma)^{59}\text{Zn}(\beta^+\nu)^{59}\text{Cu}(p,\alpha)^{56}\text{Ni}$ , can also be established. The matter flow induced by the  $^{55}\text{Ni}(p,\gamma)^{56}\text{Cu}$  reaction to bypass the  $^{56}\text{Ni}$  waiting point is illustrated in blue arrows. (All color figures in this paper are available in the online journal.)

zero-dimensional one-zone hydrodynamic XRB model, the extent of the impact the newly corrected  $^{55}\text{Ni}(p,\gamma)^{56}\text{Cu}$  reaction induces on the by-passing reaction flow, however, causes merely up to 5% difference in the productions of nuclei  $A = 55 - 65$  (Valverde et al. 2019). Moreover, due to the zero-dimensional feature of one-zone XRB model, the distribution of synthesized nuclei along the mass coordinate in the accreted envelope is unknown, and importantly, the one-zone hydrodynamic XRB model does not match with any observation.

In this work, Section 2, we present the formalism in calculating the reaction rates and the isobaric-multiplet-mass equation (Wigner 1957) that we use to determine the order of  $1_1^+$  and  $2_3^+$  (states of  $^{58}\text{Zn}$ ) dominating resonance states and to estimate the resonance energy of  $1_2^+$  resonance state. Then, the discussion of the reconstructed and newly deduced  $^{57}\text{Cu}(p,\gamma)^{58}\text{Zn}$  reaction rates are shown in Section 3. Using the one-dimensional multi-zone hydrodynamic KEPLER code (Weaver et al. 1978; Woosley et al. 2004; Heger et al. 2007), we model a set of XRB episodes matched with the GS 1826–24 burster with the newly deduced  $^{57}\text{Cu}(p,\gamma)^{58}\text{Zn}$ , Valverde et al. (2019)  $^{55}\text{Ni}(p,\gamma)^{56}\text{Cu}$ , and Kahl et al. (2019)  $^{56}\text{Ni}(p,\gamma)^{57}\text{Cu}$  reaction rates. We study the influence of these rates, and also investigate the effect of the  $^{56}\text{Ni}$ -waiting-point bypassing matter flow induced by the  $^{55}\text{Ni}(p,\gamma)^{56}\text{Cu}$  reaction. The implication of the new  $^{57}\text{Cu}(p,\gamma)^{58}\text{Zn}$ ,  $^{55}\text{Ni}(p,\gamma)^{56}\text{Cu}$ , and  $^{56}\text{Ni}(p,\gamma)^{57}\text{Cu}$  re-

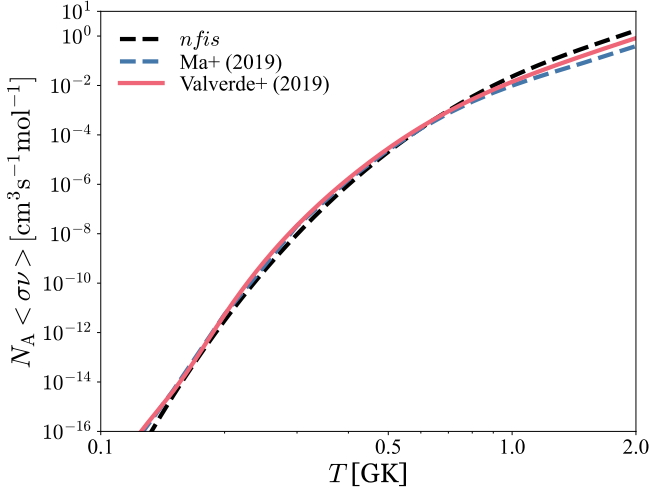


**Figure 2.** The  $^{55}\text{Ni}(p,\gamma)^{56}\text{Cu}$  thermonuclear reaction rates. Valverde et al. (2019) corrected the  $^{55}\text{Ni}(p,\gamma)^{56}\text{Cu}$  reaction rate (red solid line) after Ma et al. (2019) proposed a  $^{55}\text{Ni}(p,\gamma)^{56}\text{Cu}$  reaction rate (blue dashed line) based on the  $^{56}\text{Cu}$  proton separation energy,  $S_p(^{56}\text{Cu})=579.8$  keV, and pointed out the incorrect penetrability scaling factor implemented by Valverde et al. (2018). The Fisker et al. (2001) rate (black dashed line) is recommended by JINA REACLIB v2.2 (Cyburt et al. 2010).

action rates on XRB light curve, the nucleosyntheses in and evolution of the accreted envelope of GS 1826–24 (clocked burster) along the mass coordinate, is presented in Section 4. The conclusion of this work is given in Section 5.

## 2. REACTION RATE CALCULATIONS

The total thermonuclear proton-capture reaction rate is expressed as the sum of resonant- (res) and direct-capture (DC) on the ground state and thermally excited states in the target nucleus, and each capture with given initial and final states is weighted with its individual population factor (Fowler et al. 1964; Rolfs & Rodney 1988),

$$N_A \langle \sigma v \rangle = \sum_i (N_A \langle \sigma v \rangle_{\text{res}}^i + N_A \langle \sigma v \rangle_{\text{DC}}^i) \times \frac{(2J_i + 1)e^{-E_i/kT}}{\sum_n (2J_n + 1)e^{-E_n/kT}}, \quad (1)$$

where  $J$  are the angular momenta of initial states of target nucleus and  $E$  are the energies of these initial states.

*Resonant rates*—The resonant reaction rate for proton capture on a target nucleus in its initial state,  $i$ ,  $N_A \langle \sigma v \rangle_{\text{res}}^i$ , is a sum over all respective compound nucleus states  $j$  above the proton separation energy (Rolfs & Rodney 1988; Iliadis 2007). The resonant rate can be expressed as (Fowler et al. 1967; Schatz et al. 2005),

$$N_A \langle \sigma v \rangle_{\text{res}}^i = 1.54 \times 10^{11} (\mu T_9)^{-3/2} \times \sum_j \omega \gamma_{ij} \exp\left(-\frac{11.605 E_{\text{res}}^{ij}}{T_9}\right), \quad (2)$$

in units of  $\text{cm}^3 \text{s}^{-1} \text{mol}^{-1}$ , where the resonance energy in the center-of-mass system,  $E_{\text{res}}^{ij} = E_x^j - S_p - E_i$ , is the energy difference between the compound nucleus  $E_x^j$  state and the sum of the excitation energies of the initial state  $E_i$  and the respective proton threshold,  $S_p$ . For the capture on the ground state,  $E_i = 0$ .  $\mu$  is the reduced mass of the entrance channel in atomic mass units ( $\mu = A_T / (1 + A_T)$ , with  $A_T$  the target mass number), and  $T_9$  is the temperature in Giga Kelvin (GK). The resonance energy and strength in Eq. (2) are given in units of MeV. The resonance strength reads

$$\omega \gamma_{ij} = \frac{2J_j + 1}{2(2J_i + 1)} \frac{\Gamma_p^{ij} \times \Gamma_\gamma^j}{\Gamma_{\text{total}}^j}, \quad (3)$$

where  $J_i$  is the target spin and  $J_j$ ,  $\Gamma_p^{ij}$ ,  $\Gamma_\gamma^j$ , and  $\Gamma_{\text{total}}^j$  are a spin, proton-decay width,  $\gamma$ -decay width, and total width of the compound nucleus state  $j$ , respectively. Assuming other decay channels are closed (Audi et al. 2016) in the considered excitation energy range of the compound nuclei, the total width becomes  $\Gamma_{\text{total}}^j = \Gamma_\gamma^j + \Gamma_p^{ij}$ . Within the shell-model formalism which we use here, the proton width can be expressed as

$$\Gamma_p = \sum_{n1j} C^2 S(n1j) \Gamma_{\text{sp}}(n1j), \quad (4)$$

where  $\Gamma_{\text{sp}}$  is a single-particle width for the capture of a proton with respect to a given  $(n1j)$  quantum orbital in a spherically-symmetric mean-field potential, while  $C^2 S(n1j)$  denotes a corresponding spectroscopic factor containing information of the structure of the initial and final states. The  $\Gamma_{\text{sp}}$  can either be estimated from proton scattering cross sections in a Woods-Saxon potential with the adjusted potential depth to reproduce known proton energies (Brown 2014); or alternatively, it can also be obtained from the potential barrier penetrability calculation as (Van Wormer et al. 1994; Herndl et al. 1995),

$$\Gamma_{\text{sp}} = \frac{3\hbar^2}{\mu R^2} P_1(E), \quad (5)$$

where,  $R = r_0 \times (1 + A_T)^{1/3}$  fm (with  $r_0 = 1.25$  fm) is the nuclear channel radius; and the Coulomb barrier penetration factor  $P_1$  is

$$P_1(E) = \frac{kR}{F_1^2(E) + G_1^2(E)}, \quad (6)$$

where  $k = \sqrt{2\mu E}/\hbar$  and  $E$  is the proton energy in the center-of-mass system;  $F_1$  and  $G_1$  are the regular and irregular Coulomb functions, respectively. In the present work, we follow the same procedure as was used by Lam et al. (2016) to get the proton widths of the important  $^{57}\text{Cu}(p,\gamma)^{58}\text{Zn}$  resonances up to the Gamow window. The maximum difference between the  $\Gamma_{\text{sp}}$  described by the two methods above is below 40% for the present work.

Gamma decay widths are obtained from electromagnetic reduced transition probabilities  $B(\Omega L; J_i \rightarrow J_f)$  ( $\Omega$  stands for

electric or magnetic), which contain the nuclear structure information of the resonance states and the final bound states. The corresponding gamma decay widths for the most contributed transitions (M1 and E2) can be expressed as (Brussaard & Glaudemans 1977)

$$\begin{aligned}\Gamma_{M1} &= 1.16 \times 10^{-2} E_\gamma^3 B(M1), \text{ and} \\ \Gamma_{E2} &= 8.13 \times 10^{-7} E_\gamma^5 B(E2),\end{aligned}\quad (7)$$

where  $B(M1)$  are in  $\mu_N^2$ ,  $B(E2)$  are in  $e^2\text{fm}^4$ ,  $E_\gamma$  are in keV, while  $\Gamma_{M1}$  and  $\Gamma_{E2}$  are in units of eV. The  $B(M1)$  values have been obtained from free  $g$ -factors, i.e.,  $g_p^s=5.586$ ,  $g_n^s=-3.826$  and  $g_p^l=1$ ,  $g_n^l=0$ ; whereas the  $B(E2)$  values have been obtained from standard effective charges,  $e_p=1.5e$ , and  $e_n=0.5e$  (Honma et al. 2004). We use experimental energies,  $E_\gamma$ , when available. The total electromagnetic decay width is obtained from the summation of all partial decay widths for a given initial state.

*Information of nuclear structure*—The essential information needed to estimate the resonant rate contribution of  $^{57}\text{Cu}(p,\gamma)^{58}\text{Zn}$  consists of the resonance energies of the compound nucleus  $^{57}\text{Cu}+p$ , one-proton transfer spectroscopic factors, and proton- and gamma-decay widths. The properties of resonances sensitive to the  $^{57}\text{Cu}(p,\gamma)^{58}\text{Zn}$  reaction rate of XRB temperature range are provided by Langer et al. (2014). Nevertheless, the order of the  $1_1^+$  and  $2_3^+$  states of  $^{58}\text{Zn}$  were undetermined by Langer et al. In order to reproduce Langer et al. rate, we find that the dominant resonances for the temperature range from 1 to 2 GK sensitive to XRB are not limited to the measured  $2_4^+$  state. The  $1_2^+$  and  $2_5^+$  resonance states, which were not observed by Langer et al., also contribute to the total reaction rate at temperature  $1 \lesssim T(\text{GK}) \lesssim 2$ .

In the present study, we use the isobaric multiplet mass equation (IMME) (Wigner 1957) to determine the energies of experimentally unknown, but important resonance state in  $^{58}\text{Zn}$ , i.e., the order of the  $1_1^+$  and  $2_3^+$  states of  $^{58}\text{Zn}$  and the energy of  $1_2^+$  state. A similar method was exploited earlier by Richter et al. (2011, 2012, 2013) to provide missing experimental information of the nuclear level schemes. Also, the same method was used by Schatz & Ong (2017) to estimate the unknown nuclear masses important for reverse  $(p,\gamma)$  rates. Assuming that the isospin-symmetry breaking forces are two-body operators of the isovector and isotensor character, the mass excesses of the members of an isobaric multiplet ( $I=1, I_z=-I, -I+1, \dots, I$ ) show at most a quadratic dependence on  $I_z$ , as expressed by the IMME (Wigner 1957),

$$M_{I_z}(\alpha, I) = a(\alpha, I) + b(\alpha, I)I_z + c(\alpha, I)I_z^2, \quad (8)$$

where  $M_{I_z}(\alpha, I)$  is the mass excess of a quantum state of isospin  $(I, I_z)$ , and  $\alpha = (A, J^\pi, N_{\text{exc}}, \dots)$  are the nuclear mass number  $A$ , excited state number  $N_{\text{exc}}$ , and all other quantum numbers labeling the quantum state. The  $a$ ,  $b$ , and  $c$  coefficients reflect contributions from the isoscalar, isovector, and isotensor parts of the effective nucleon-nucleon interaction, respectively (see Ormand & Brown (1989) or Lam et

al. (2013a,b) for the detailed notation and formalism). For an isobaric-triplet states ( $I=1, I_z=-1, 0, +1$ ), we can form from Eq. (8) a system of three linear equations, and therefore, express the IMME  $c$  coefficient in terms of three mass excesses as

$$c = [M_{-1}(\alpha, 1) + M_{+1}(\alpha, 1) - 2M_0(\alpha, 1)]/2. \quad (9)$$

In turn, if we know the mass excesses of  $I_z=0$  and  $I_z=1$  isobaric multiplet members and a theoretical  $c$  coefficients, the mass excess of a proton-rich member ( $I_z=-1$ ) can be found via a simple relation:

$$M_{-1}(\alpha, 1) = 2M_0(\alpha, 1) - M_{+1}(\alpha, 1) + 2c(\alpha, 1). \quad (10)$$

This equation defines the method which we use in the present paper.

We first obtain a set of theoretical IMME  $c$  coefficients for the lowest and excited  $A=58$  triplets, including those which involve the dominant resonances. To this end, we perform large-scale shell-model calculations in full  $pf$  shell-model space using the NuShellX@MSU shell-model code (Brown & Rae 2014) with the charge-dependent Hamiltonian, which is constructed from the modern isospin-conserving Hamiltonian (GXPF1a; Honma et al. 2004, 2005), the two-body Coulomb interaction, strong charge-symmetry-breaking and charge-independence-breaking terms (Ormand & Brown 1989), and the  $pf$  shell-model space isovector single-particle energies (Ormand & Brown 1995). The Hamiltonian is referred to as ‘‘cdGX1A’’ and was used by Smirnova et al. (2016, 2017) to investigate the isospin mixing in  $\beta$ -delayed proton emission of  $pf$ -shell nuclei. The IMME  $c$  coefficients of these dominant resonances permit us to determine the order of  $1_1^+$  and  $2_3^+$  states of  $^{58}\text{Zn}$  and to estimate the resonance energy of the  $1_2^+$  resonance state. Properties of all other resonances situated within the Gamow window corresponding to the XRB temperature range are computed using the KShell code (Shimizu et al. 2019) in a full  $pf$  shell-model space with the GXPF1a Hamiltonian. For  $A=57$  and  $58$ , Hamiltonian matrices of dimensions up to  $1.58 \times 10^9$  have been diagonalized using thick-restart block Lanczos method.

The theoretical IMME  $c$  coefficients are then compared with the available experimental data compiled in Lam et al. (2013b) and updated in the present work by the recently re-evaluated mass excesses of  $^{58}\text{Zn}$ ,  $^{58}\text{Cu}$ , and  $^{58}\text{Ni}$  (Audi et al. 2016; AME2016). For excited multiplets, the experimental information on level schemes have been taken from Langer et al. (2014) for  $^{58}\text{Zn}$ , from Rudolph & McGrath (1973); Rudolph et al. (1998, 2000) for  $^{58}\text{Cu}$ , and from Jongsma et al. (1972); Honkanen et al. (1981); Johansson et al. (2009); Rudolph et al. (2002) for  $^{58}\text{Ni}$ . The uncertainty of the measured  $^{58}\text{Zn}$  mass (Seth et al. 1986) dominates the experimental IMME  $c$  coefficients uncertainties and propagates to the proton separation energy of  $^{58}\text{Zn}$ ,  $S_p(^{58}\text{Zn})=2.280 \pm 0.050$  MeV (AME2016). In general, theoretical  $c$  coefficients are seen to be in robust agreement with the respective experimental values. The comparison yields root-mean-square (rms) deviation of about 22 keV, which we



**Table 1.** Experimental isospin  $I=1$  states in  $^{58}\text{Zn}$ ,  $^{58}\text{Cu}$ , and  $^{58}\text{Ni}$  organized in isobaric multiplets and the corresponding experimental and theoretical IMME  $c$  coefficients. Tentatively spin and parity assignments are proposed on the basis of the IMME theory for the states (bold texts) without firm experimental assignments.

$J_i^\pi$	$E_x$ [keV] <sup>a,b</sup>		$^{58}\text{Ni}$	IMME $c$ [keV]	
	$^{58}\text{Zn}$	$^{58}\text{Cu}$		Exp. <sup>b</sup>	Theo. <sup>c</sup>
$0_1^+$	0	203	0	200 (25)	235 (22)
$2_1^+$	1356 (3)	1653	1454	156 (25)	179 (22)
$4_1^+$	2499 (4)	2750	2459	133 (25)	154 (22)
$2_2^+$	2609 (6)	2931	2775	166 (25)	162 (22)
$1_1^+$ <sup>d</sup>	2861 (4)	~3100 – ~3200	2902		133 (22)
<b><math>2_3^+</math></b> <sup>d</sup>	2904 (5)		3038		192 (22)
$2_4^+$	3265 (6)	3513	3264	156 (25)	143 (22)
$3_1^+$	3378 (5)		3421		141 (22)
<b><math>1_2^+</math></b>		~3900 – ~4100	3594		142 (22)
<b><math>2_5^+</math></b>			3898		161 (22)

NOTE—

<sup>a</sup> Only uncertainties of (or more than) 1 keV based on the evaluation of Nesaraja et al. (2010) are shown.

<sup>b</sup> Presently compiled from the evaluated nuclear masses (AME2016), and experimentally measured levels (Jongsma et al. 1972; Honkanen et al. 1981; Rudolph & McGrath 1973; Rudolph et al. 1998, 2000, 2002; Johansson et al. 2009; Langer et al. 2014) according to the procedure implemented by Lam et al. (2013b).

<sup>c</sup> Presently calculated with the cdGX1A Hamiltonian based on the full  $pf$  shell-model space. The  $1_1^+$ ,  $2_3^+$ ,  $3_1^+$ ,  $1_2^+$ , and  $2_5^+$  triplets are not taken into comparison yielding the rms.

<sup>d</sup> An alternative order of the  $1_1^+$  and  $2_3^+$  states according to IMME dominance to the previous order proposed by Langer et al. (2014).

assign as theoretical uncertainty to the calculated values, see Table 1.

According to the recent compilation of IMME  $c$  coefficients of isobaric multiplets with  $A = 6 - 58$  (Lam et al. 2013b), the IMME  $c$  coefficients exhibit a gradually decreasing trend as a function of  $A$  with values ranging between about 400 and 150 keV. As is well known from the data, the  $c$  coefficients of triplets show a prominent staggering effect, being split in two families: the values of  $c$  coefficients inherent to isobars with  $A=4n+2$  appear to be systematically higher than those for their  $A=4n$  neighbors with  $n$  being a positive integer. These average values decrease with increasing  $A$  approximately as  $A^{-1/3}$  as suggested by a uniformly charge liquid drop model. It has also been noticed that the amplitude of staggering decreases with increasing excitation energy manifesting the weakening of the pairing effects in higher excited states (Lam et al. 2013a). In the present study, we extend the compilation of Lam et al. (2013b) and tentatively propose excited isobaric multiplets in the  $A=58$  triplet. Although the dependence of  $c$  coefficients on excitation energy is less known, from theoretical studies in the  $sd$ -shell nuclei, the amplitude of staggering in isobaric triplets is expected to gradually diminish in the  $pf$ -shell nuclei. Recently, more precise nuclear mass measurements confirmed the persistence of these trend in the  $pf$ -shell nuclei (Zhang et al. 2018; Surbrook et al. 2019; Fu et al. 2020). We find that

the values of  $c$  coefficients provide a very stringent test for isobaric multiplets as we will see below.

*The order of  $1_1^+$  and  $2_3^+$  states.* As was mentioned before, the order of  $1_1^+$  and  $2_3^+$  states stays undetermined in the work by Langer et al. (2014) with two plausible energies, 2861 keV and 2904 keV. The character of electromagnetic decay of those states weakly supports the assignment proposed in that work, that the lower state is a  $2_3^+$  state and the higher one is the  $1_1^+$ ,  $I=1$  state. Indeed, we can get the ratio of the partial electromagnetic widths for the decay of these states to the  $0_{g.s.}^+$  and  $2_1^+$  to be more in reasonable agreement with that assignment as seen from Table 2.

Alternatively, a certain constraint can also be imposed by the IMME. Although the  $1_1^+$  and  $2_3^+$ ,  $I = 1$  states of  $^{58}\text{Cu}$  are not assigned (Nesaraja et al. 2010), from the existing data we find that the best candidate for  $2_3^+$  could be a state at  $3230 \pm 20$  keV as measured by Rudolph & McGrath (1973) based on the ( $^3\text{He},t$ ) reaction on the  $^{58}\text{Ni}$  target. Taking into account the  $2_3^+$  ( $3037.86 \pm 0.16$  keV) state of  $^{58}\text{Ni}$  (Nesaraja et al. 2010), we check for plausible values of the corresponding  $c$  coefficients assuming both states of question in  $^{58}\text{Zn}$ ; we then obtain  $c = 145 \pm 32$  keV assuming 2904 keV, or  $c = 124 \pm 32$  keV assuming 2861 keV for the  $2_3^+$  of  $^{58}\text{Zn}$ . With the theoretical uncertainties of  $c$  coefficients, 22 keV (Table 1), we propose the 2904-keV state could be tentatively assigned as  $2_3^+$ .

For  $1_1^+$ ,  $I = 1$  state in  $^{58}\text{Cu}$ , only an interval of energies can be proposed. Indeed, no low-lying  $1^+$ ,  $I = 1$  states have been observed by Fujita et al. (2002) and by Fujita et al. (2007). To understand this fact, we have calculated a Gamow-Teller (GT) strength distribution from the  $^{58}\text{Ni}$  ground state to the  $1^+$  states in  $^{58}\text{Cu}$  using the GXPF1A Hamiltonian. The results are summarized in Table 3. First, we remark that there is a relatively good agreement with the data found in Fujita et al. (2002) and in Fujita et al. (2007). For example, the  $B(\text{GT})$  values of  $1^+$ ,  $I = 0$  at low energies are comparable. In particular, we find also large intensities populated two lowest states, as well as our calculation reproduces a relatively large strength fragment at 3.4 MeV which may be split between two states in experiment. Second, it can be noticed that the two lowest  $1^+$ ,  $I = 1$  states carry a very little amount of the GT strength, similar to what Fujita et al. (2007) found also using the KB3G Hamiltonian (Poves et al. 2001). It is therefore well probably that those states either were not observed by charge-exchange experiments, or correspond to low statistic counts at around 3.1 – 3.2 MeV in Fig. 5 of Fujita et al. (2007). With the tentative assignment of the  $2_3^+$  of  $^{58}\text{Zn}$  above, we propose an alternative assignment as compared to the work of Langer et al. (2014), and hence the 2861-keV state could be proposed as  $1_1^+$ .

We note that the inverse assignment of the  $1_1^+$  and  $2_3^+$  states compared to Langer et al. (2014) assignment, in fact, changes the contributions of the  $1_1^+$  and  $2_3^+$  resonance states. This is mainly because the main contributions for the  $2_3^+$  and  $1_1^+$  states are the  $p_{3/2}$  and  $f_{5/2}$  particle captures, respectively. Once the  $1^+$  state is assigned with the lower excitation en-

**Table 2.** Experimental decay intensities and theoretical partial widths for electromagnetic decay of the states at 2861 keV and 2904 keV in  $^{58}\text{Zn}$ .

$J_i^\pi$	$E_x$ [keV]	Partial electromagnetic widths, $\Gamma_\gamma$ [meV]	
		$J_i^\pi \rightarrow 0_{\text{g.s.}}^+$	$J_i^\pi \rightarrow 2_1^+$
$2_3^+$	2861	2.18	3.12
$1_1^+$	2904	0.34	7.5
$1_1^+$	2861	0.33	7.0
$2_3^+$	2904	2.35	3.38

	$E_x$ [keV]	Electromagnetic decay intensities, $I_\gamma$ [%]	
		$J_i^\pi \rightarrow 0_{\text{g.s.}}^+$	$J_i^\pi \rightarrow 2_1^+$
Exp.	2861	7 (2)	8 (2)
Exp.	2904	3 (1)	13 (2)

**Table 3.** Theoretical Gamow-Teller strength,  $B(\text{GT})$ , populating the  $1^+$  states in  $^{58}\text{Cu}$  deduced from the cdGX1A Hamiltonian.

Isospin, $I$	$E_x$ [keV]	Gamow-Teller strengths, $B(\text{GT})^a$
0	0.000	0.221
0	1.135	0.190
0	2.181	0.013
0	2.782	0.024
1	3.298	0.001
0	3.353	0.002
0	3.426	0.217
0	3.550	0.000
1	3.612	0.020
0	3.767	0.015
0	3.860	0.076
0	4.321	0.005
0	4.565	0.051
0	4.871	0.151
0	5.035	0.081
0	5.130	0.010
0	5.260	0.023
0	5.358	0.028
0	5.491	0.003
0	5.528	0.000

NOTE—

<sup>a</sup> The theoretical  $B(\text{GT})$  is quenched with the standard quenching factor of 0.77 (Horoi et al. 2007).

ergy and much larger suppression for the  $f$ -wave resonance, the  $\Gamma_p$  of the  $1_1^+$  resonance state decreases, causing the contribution of  $1_1^+$  resonance state to the total resonance rate being much reduced.

*The energies of  $1_2^+$  and  $2_5^+$  states.* The predicted  $B(\text{GT})$  intensity to this state by theory could, in principle, have been seen in the data of the charge-exchange experiment performed by Fujita et al. (2007). Three possible candidates have been reported between 3.6 and 4 MeV as can be seen from Figs. 5 and 7 of that article. Taking any of them and using the theoretically predicted IMME  $c$  coefficient of ( $A=58$ ,  $1_2^+$ ,  $I=1$ ) triplet,  $142 \pm 22$  keV, we estimate that the energy of the  $^{58}\text{Zn}$ ,  $1_2^+$  state cannot be below about  $3664 \pm 22$  keV. The uncertainty is based on the comparison presented in Table 1. This IMME estimated  $1_2^+$  state is  $309 \pm 22$  keV higher than the one estimated by using GXPF1A Hamiltonian that was used by Langer et al. (2014) to obtain the contribution from the  $1_2^+$  resonance state for the  $^{57}\text{Cu}(p,\gamma)^{58}\text{Zn}$  reaction rate.

There is no best candidate  $2_5^+$  isobaric analogue state in  $^{58}\text{Cu}$  to estimate the  $2_5^+$  state of  $^{58}\text{Zn}$ . The GXPF1a Hamiltonian predicts the  $2_5^+$  state to be at 3605 keV excitation energy and we adopt this value as a lower limit for  $^{58}\text{Zn}$ , being aware that in the mirror nucleus,  $^{58}\text{Ni}$ , its analogue is found at 3.898 MeV. Applying the theoretical IMME  $c$  coefficient of ( $A=58$ ,  $2_5^+$ ,  $I=1$ ) triplet,  $161 \pm 22$  keV, we can expect that the  $2_5^+$ ,  $I=1$  state in  $^{58}\text{Zn}$  to be in the energy interval of 3.9 – 4.1 MeV. Future high precision experiment measuring the level schemes of  $^{58}\text{Cu}$  and  $^{58}\text{Zn}$  in this energy region may provide more information of the  $1_1^+$ ,  $1_2^+$ , and  $2_5^+$  isobaric analogue states, and the  $1_2^+$  and  $2_5^+$  states of  $^{58}\text{Zn}$ .

By comparing the  $\Gamma_\gamma^{2_3^+}$  produced from the full  $pf$ -model space used in the present work with the  $\Gamma_\gamma^{2_3^+}$  generated from the four-particle-four-hole truncated scheme used in Langer et al. (2014) calculation, we notice that the present  $\Gamma_\gamma^{2_3^+}$  of  $^{58}\text{Zn}$  (Table 4) is one order of magnitude lower than the one calculated by Langer et al. (2014). Nevertheless, the respective  $\Gamma_p$  is two orders of magnitude lower than  $\Gamma_\gamma^{2_3^+}$ , and thus, such difference in the  $\Gamma_\gamma^{2_3^+}$  state does not impact the respective  $\omega\gamma$ .

With the information of nuclear structure described above, we deduce a set of resonance properties of  $^{58}\text{Zn}$  to construct the new  $^{57}\text{Cu}(p,\gamma)^{58}\text{Zn}$  resonant reaction rate within the typical XRB temperature range, particularly the GS 1826–24 burster. We only consider the proton-capture on the  $3/2_{\text{g.s.}}^-$  ground state (g.s.) of  $^{57}\text{Cu}$  as the contribution from proton resonant captures on thermally excited states of  $^{57}\text{Cu}$  are negligible due to rather high lying excited states. Hence, it is adequate to just present the newly deduced resonance properties of  $^{57}\text{Cu}(p,\gamma)^{58}\text{Zn}$  reaction rate up to the  $3_7^+$  state (5.250 MeV) in Table 4 within the Gamow window corresponding to the XRB temperature range.

*Direct-capture rate*—Comparing the direct-capture rate deduced by Fisker et al. (2001) (or by Forstner et al. 2001) with the presently deduced resonant capture rate, we notice that the contribution of direct capture is exponentially lower than the contribution of the dominating resonances throughout XRB related temperature range from 0.3 to 2 GK. Hence, the contribution of the direct-capture rate is negligible for the  $^{57}\text{Cu}(p,\gamma)^{58}\text{Zn}$  reaction rate, see Fig. 3 which only presents Fisker et al. direct-capture rate.

### 3. NEW $^{57}\text{Cu}(p,\gamma)^{58}\text{Zn}$ REACTION RATE

Table 5 shows the presently calculated total reaction rate of  $^{57}\text{Cu}(p,\gamma)^{58}\text{Zn}$  as a function of temperature. The present (*Present*, hereafter) thermonuclear rates are parameterized by the format proposed by Rauscher & Thielemann (2000) with the expression below,

$$N_A \langle \sigma v \rangle = \sum_i \exp(a_0^i + \frac{a_1^i}{T_9} + \frac{a_2^i}{T_9^{1/3}} + a_3^i T_9^{1/3} + a_4^i T_9 + a_5^i T_9^{5/3} + a_6^i \ln T_9). \quad (11)$$

**Table 4.** Properties of  $^{58}\text{Zn}$  for the ground-state proton capture in the present  $^{57}\text{Cu}(p,\gamma)^{58}\text{Zn}$  resonant rate calculation.

$J_i^\pi$	$E_x$ [MeV]	$E_{\text{res}}$ [MeV] <sup>c</sup>	$C^2S_{7/2}$ ( $l=3$ )	$C^2S_{3/2}$ ( $l=1$ )	$C^2S_{5/2}$ ( $l=3$ )	$C^2S_{1/2}$ ( $l=1$ )	$\Gamma_\gamma$ [eV]	$\Gamma_p$ [eV]	$\omega\gamma$ [eV]
$0_1^+$	0.000			1.1001			—		
$2_1^+$	1.356 <sup>a</sup>		0.0351	0.8381	0.1459	0.0913	$6.736 \times 10^{-4}$		
$4_1^+$	2.499 <sup>a</sup>	0.219	0.0123		0.6737		$1.741 \times 10^{-4}$	$1.002 \times 10^{-17}$	$1.127 \times 10^{-17}$
$2_2^+$	2.609 <sup>a</sup>	0.329 <sup>d</sup>	0.0027	0.5776	0.0063	0.1144	$9.034 \times 10^{-3}$	$1.695 \times 10^{-10}$	$1.059 \times 10^{-10}$
$1_1^+$	2.861 <sup>a</sup>	0.581 <sup>d</sup>		0.0000	0.6522	0.0867	$7.300 \times 10^{-3}$	$4.662 \times 10^{-6}$	$1.747 \times 10^{-6}$
$2_3^+$	2.904 <sup>a</sup>	0.624 <sup>d</sup>	0.0020	0.0131	0.0103	0.1649	$5.278 \times 10^{-3}$	$3.380 \times 10^{-5}$	$2.099 \times 10^{-5}$
$0_2^+$	2.995	0.715		0.4393			$4.758 \times 10^{-5}$	$1.097 \times 10^{-3}$	$5.700 \times 10^{-6}$
$4_3^+$	3.263	0.983	0.0016		0.0048		$3.589 \times 10^{-4}$	$1.074 \times 10^{-5}$	$1.173 \times 10^{-5}$
$2_4^+$	3.265 <sup>a</sup>	0.985 <sup>d</sup>	0.0005	0.1174	0.4953	0.0002	$4.131 \times 10^{-3}$	$4.338 \times 10^{-2}$	$2.357 \times 10^{-3}$
$0_3^+$	3.349	1.069		0.0419			$8.758 \times 10^{-4}$	$4.827 \times 10^{-2}$	$1.075 \times 10^{-4}$
$3_1^+$	3.378 <sup>a</sup>	1.098	0.0016	0.0000	0.6849		$3.466 \times 10^{-3}$	$4.649 \times 10^{-3}$	$1.737 \times 10^{-3}$
$2_5^+$	3.605	1.325	0.0012	0.0011	0.0302	0.2498	$1.387 \times 10^{-2}$	3.677	$8.637 \times 10^{-3}$
$1_2^+$	3.664 <sup>b</sup>	1.384 <sup>d</sup>		0.0000	0.1011	0.5980	$4.526 \times 10^{-2}$	$1.527 \times 10^{+1}$	$1.692 \times 10^{-2}$
$3_2^+$	3.670	1.390	0.0042	0.0000	0.0033		$3.680 \times 10^{-4}$	$1.745 \times 10^{-3}$	$2.659 \times 10^{-4}$
$4_3^+$	3.969	1.689	0.0169		0.0077		$1.275 \times 10^{-2}$	$6.250 \times 10^{-2}$	$1.191 \times 10^{-2}$
$5_1^+$	4.009	1.729	0.0012				$5.162 \times 10^{-4}$	$4.589 \times 10^{-3}$	$6.380 \times 10^{-4}$
$2_6^+$	4.077	1.797	0.0000	0.0019	0.0030	0.0671	$2.016 \times 10^{-3}$	$3.024 \times 10^{+1}$	$1.260 \times 10^{-3}$
$3_3^+$	4.168	1.888	0.0192	0.0020	0.0312		$1.202 \times 10^{-2}$	2.044	$1.046 \times 10^{-2}$
$0_4^+$	4.188	1.908	0.0079		0.0087		$1.430 \times 10^{-3}$	$1.468 \times 10^{-1}$	$1.593 \times 10^{-3}$
$4_4^+$	4.242	1.962		0.0000			$8.661 \times 10^{-3}$	0.000	0.000
$4_5^+$	4.268	1.988	0.0034		0.0584		$1.323 \times 10^{-2}$	$6.240 \times 10^{-1}$	$1.458 \times 10^{-2}$
$2_7^+$	4.270	1.990	0.0035	0.0007	0.0357	0.0001	$3.740 \times 10^{-3}$	1.477	$2.332 \times 10^{-3}$
$0_5^+$	4.363	2.083		0.0198			$1.606 \times 10^{-2}$	$4.158 \times 10^{+1}$	$2.007 \times 10^{-3}$
$4_6^+$	4.520	2.240	0.0051		0.0000		$6.485 \times 10^{-3}$	$3.290 \times 10^{-1}$	$7.154 \times 10^{-3}$
$3_4^+$	4.546	2.266	0.0003	0.0000	0.0016		$3.161 \times 10^{-2}$	$7.852 \times 10^{-2}$	$1.972 \times 10^{-2}$
$5_2^+$	4.594	2.314	0.0065				$7.146 \times 10^{-3}$	$5.545 \times 10^{-1}$	$9.701 \times 10^{-3}$
$3_5^+$	4.653	2.373	0.0003	0.0000	0.0000		$1.428 \times 10^{-2}$	$3.279 \times 10^{-2}$	$8.705 \times 10^{-3}$
$2_8^+$	4.708	2.428	0.0092	0.0000	0.0323	0.0059	$2.609 \times 10^{-2}$	$4.483 \times 10^{+1}$	$1.630 \times 10^{-2}$
$4_7^+$	4.832	2.552	0.0050		0.0050		$1.378 \times 10^{-2}$	1.715	$1.538 \times 10^{-2}$
$5_3^+$	4.909	2.629	0.0001				$1.751 \times 10^{-3}$	$2.902 \times 10^{-2}$	$2.271 \times 10^{-3}$
$4_8^+$	4.964	2.684	0.0000		0.0090		$2.452 \times 10^{-3}$	1.692	$2.755 \times 10^{-3}$
$2_9^+$	5.013	2.733	0.0002	0.0027	0.0002	0.0022	$3.656 \times 10^{-3}$	$9.118 \times 10^{+1}$	$2.285 \times 10^{-3}$
$3_6^+$	5.040	2.760	0.0060	0.0000	0.0006		$1.759 \times 10^{-2}$	2.944	$1.530 \times 10^{-2}$
$4_9^+$	5.184	2.904	0.0073		0.0037		$2.096 \times 10^{-2}$	6.858	$2.351 \times 10^{-2}$
$5_4^+$	5.208	2.928	0.0001				$7.299 \times 10^{-3}$	$7.758 \times 10^{-2}$	$9.173 \times 10^{-3}$
$2_{10}^+$	5.227	2.947	0.0001	0.0327	0.0016	0.0023	$2.958 \times 10^{-2}$	$1.230 \times 10^{+3}$	$1.849 \times 10^{-2}$
$3_7^+$	5.250	2.970	0.0001	0.0008	0.0002		$1.045 \times 10^{-2}$	$2.904 \times 10^{+1}$	$9.142 \times 10^{-3}$

NOTE—

<sup>a</sup> The experimentally determined energy levels of  $^{58}\text{Zn}$  (Langer et al. 2014).<sup>b</sup> The theoretical energy levels of  $^{58}\text{Zn}$  predicted from IMME and obtained from the present full  $pf$ -model space shell-model calculation with cdGX1A Hamiltonian, see text.<sup>c</sup> Calculated by  $E_{\text{res}} = E_x - S_p - E_i$  with  $S_p(^{58}\text{Zn})=2.280\pm 0.050$  MeV deduced from AME2016 (Audi et al. 2016).<sup>d</sup> Resonances dominantly contributing to the total rate within temperature region of 0.1–2 GK.

These parameters, i.e.,  $a_0, a_1, a_2, a_3, a_4, a_5$ , and  $a_6$  are listed in Table 6. The parameterized *Present* rate is evaluated according to an accuracy quantity proposed by Rauscher & Thielemann (2000),

$$\zeta = \frac{1}{n} \sum_{i=1}^n \left( \frac{r_i - f_i}{f_i} \right)^2,$$

where  $n$  is the number of data points,  $r_i$  are the original *Present* rate calculated for each respective temperature, and  $f_i$  are the fitted rate at that temperature. With  $n=297$ ,  $\zeta$  is  $4.45 \times 10^{-3}$ , and the fitting error is 5.90% for the temperature range from 0.01 GK to 3 GK. The parameterized rate is obtained with aid from the Computational Infrastructure for Nuclear Astrophysics (CINA; Smith et al. 2004). For

the rate above 3 GK, one may refer to statistical model calculations to match with the *Present* rate, which is only valid within the mentioned temperature range and fitting errors, see NACRE (Angulo et al. 1999).

We reproduce Langer et al. rate (Langer et al. 2014) with taking into account of the contributions from the  $1_2^+, 2_4^+$ , and  $2_5^+$  resonance states, which are dominant at temperature region  $0.8 \lesssim T(\text{GK}) \lesssim 2$ , see the top panel in Fig. 3. Other contributing resonances to Langer et al. rate for temperature  $T \lesssim 0.8$  GK are also included in Fig. 3. The *Present* rate and the respective main contributing resonances with updated  $\Gamma_p$  and  $\Gamma_\gamma$  widths based on a full  $pf$ -model space are plotted in the bottom panel of Fig. 3. We find that the new resonance energy estimated from IMME formalism reduces the contri-

**Table 5.** Thermonuclear reaction rates of  $^{57}\text{Cu}(p,\gamma)^{58}\text{Zn}$ .

$T_9$	centroid [ $\text{cm}^3\text{s}^{-1}\text{mol}^{-1}$ ]	lower limit [ $\text{cm}^3\text{s}^{-1}\text{mol}^{-1}$ ]	upper limit [ $\text{cm}^3\text{s}^{-1}\text{mol}^{-1}$ ]
0.1	$1.44 \times 10^{-20}$	$1.28 \times 10^{-21}$	$6.62 \times 10^{-20}$
0.2	$9.72 \times 10^{-13}$	$2.39 \times 10^{-13}$	$1.62 \times 10^{-12}$
0.3	$1.23 \times 10^{-9}$	$6.53 \times 10^{-10}$	$2.78 \times 10^{-9}$
0.4	$2.34 \times 10^{-7}$	$2.19 \times 10^{-7}$	$2.93 \times 10^{-7}$
0.5	$6.08 \times 10^{-6}$	$4.23 \times 10^{-6}$	$9.30 \times 10^{-6}$
0.6	$5.45 \times 10^{-5}$	$3.08 \times 10^{-5}$	$9.90 \times 10^{-5}$
0.7	$2.80 \times 10^{-4}$	$1.40 \times 10^{-4}$	$5.60 \times 10^{-4}$
0.8	$1.05 \times 10^{-3}$	$5.08 \times 10^{-4}$	$2.16 \times 10^{-3}$
0.9	$3.22 \times 10^{-3}$	$1.61 \times 10^{-3}$	$6.43 \times 10^{-3}$
1.0	$8.42 \times 10^{-3}$	$4.50 \times 10^{-3}$	$1.60 \times 10^{-2}$
1.1	$1.94 \times 10^{-2}$	$1.11 \times 10^{-2}$	$3.46 \times 10^{-2}$
1.2	$3.99 \times 10^{-2}$	$2.43 \times 10^{-2}$	$6.72 \times 10^{-2}$
1.3	$7.51 \times 10^{-2}$	$4.81 \times 10^{-2}$	$1.20 \times 10^{-1}$
1.4	$1.31 \times 10^{-1}$	$8.73 \times 10^{-2}$	$2.00 \times 10^{-1}$
1.5	$2.13 \times 10^{-1}$	$1.48 \times 10^{-1}$	$3.14 \times 10^{-1}$
1.6	$3.30 \times 10^{-1}$	$2.35 \times 10^{-1}$	$4.70 \times 10^{-1}$
1.7	$4.86 \times 10^{-1}$	$3.56 \times 10^{-1}$	$6.76 \times 10^{-1}$
1.8	$6.89 \times 10^{-1}$	$5.15 \times 10^{-1}$	$9.36 \times 10^{-1}$
1.9	$9.44 \times 10^{-1}$	$7.19 \times 10^{-1}$	1.26
2.0	1.26	$9.71 \times 10^{-1}$	1.65

bution of the  $1_2^+$  resonance state, becoming lower than the contribution of the  $2_4^+$  resonance state.

The comparison of the *Present* rate with Langer et al. rate and with other reaction rates compiled into JINA REACLIB v2.2 by Cyburt et al. (2010) is shown in Fig. 4. The Hauser-Feshbach statistical model rates, i.e. *rath*<sup>1</sup>, *thra*<sup>2</sup>, and *ths8*<sup>3</sup> are very close to one another from 0.1 to 2.0 GK, and they are lower than the *Present* rate up to an order of magnitude at temperature  $T \lesssim 0.9$  GK. The *Present* rate is up to a factor of two lower than Langer et al. rate from 0.8 to 2 GK covering the typical maximum temperature of GS 1826–24 burster, and up to a factor of five lower than the *wien2* rate (Forstner et al. 2001) recommended by JINA REACLIB v2.2, see the comparison in the respective ratio in the bottom panel of Fig. 4.

By taking into account the uncertainty of  $S_p(^{58}\text{Zn})$ , we estimate and list the uncertainty of *Present*  $^{57}\text{Cu}(p,\gamma)^{58}\text{Zn}$  reaction rate as upper and lower limits in Table 5. Both upper and lower limits are shown as red zone in Fig. 4, whereas the uncertainty of Langer et al. rate is indicated as blue zone. Even if the uncertainty due to the order of  $1_1^+$  and  $2_3^+$  states would have been removed, the uncertainty of  $S_p(^{58}\text{Zn})$  propagated from the measured  $^{58}\text{Zn}$  mass (Seth et al. 1986) is still dominant and persistent. Note that this is the first  $^{57}\text{Cu}(p,\gamma)^{58}\text{Zn}$  reaction rate constructed from important experimental information supplemented with the full *pf*-shell space shell-model calculation that yields converged resonance energies,  $\Gamma_\gamma$ , and spectroscopic factors; and the uncertainty is clearly identified, whereas the Hauser-Feshbach statistical model rates may include unknown systematic er-

<sup>1</sup> Produced by Rauscher & Thielemann (2000) using NON-SMOKER code with FRDM mass input (Möller et al. 1995).

<sup>2</sup> *Ibid.*, with ETFSI-Q mass input (Pearson et al. 1996).

<sup>3</sup> Produced by T. Rauscher using NON-SMOKER code as part of JINA REACLIB since the v1.0 release (Cyburt et al. 2010).

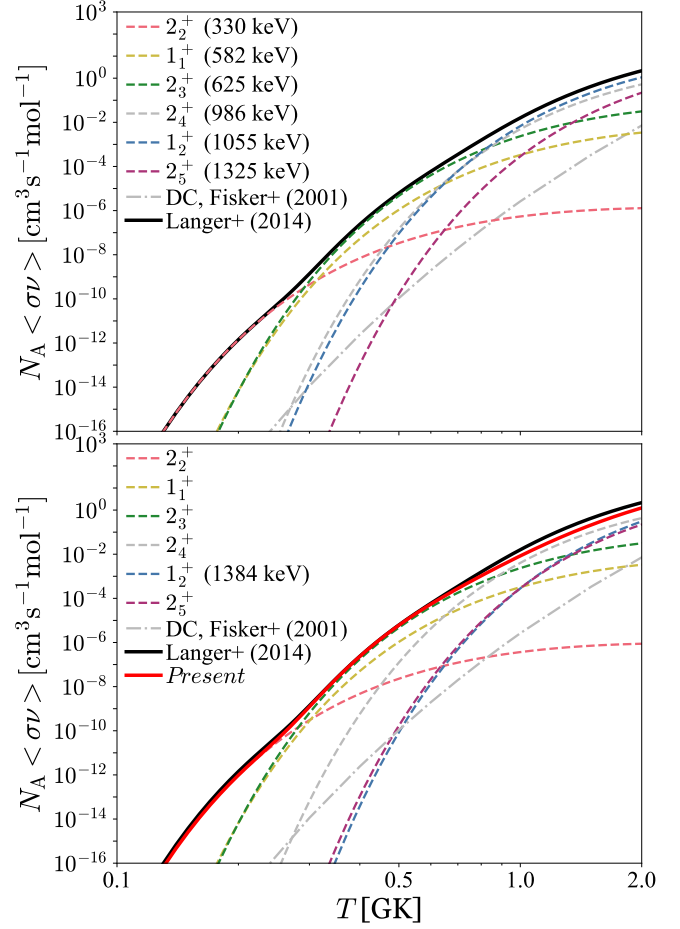


**Figure 3.** The  $^{57}\text{Cu}(p,\gamma)^{58}\text{Zn}$  thermonuclear reaction rates. Top Panel: The main contributing resonances of proton captures on the  $3/2_{g.s.}^-$  state of  $^{57}\text{Cu}$  in the temperature region of XRB interest are indicated as dashed color lines with the respective resonance energies. Bottom Panel: The updated main contributing resonances with full *pf* shell-model space calculation for  $\Gamma_\gamma$  widths and spectroscopic factors, and with the resonance energy of the  $1_2^+$  state using IMME formalism. See details in the text and Table 4.

rors because of their limited capability in estimating level densities of nuclei near to the proton drip line.

#### 4. IMPLICATION ON MULTI-ZONE X-RAY BURST MODELS

We explore the influence of the *Present*  $^{57}\text{Cu}(p,\gamma)^{58}\text{Zn}$  reaction rate on characterizing the XRB light curves of the GS 1826–24 X-ray source (Makino et al. 1988; Tanaka et al. 1989) and burst-ash composition after an episode of XRBs based on one-dimensional multi-zone hydrodynamic XRB models. The theoretical XRB models matched with the GS 1826–24 clocked burster (Ubertini et al. 1999) are instantiated by the KEPLER code (Weaver et al. 1978; Woosley et al. 2004; Heger et al. 2007) and were used by Heger et al. (2007) to perform the first quantitative comparison with the observed GS 1826–24 light curve. Later, the GS 1826–24



**Table 6.** Parameters of  $^{57}\text{Cu}(p,\gamma)^{58}\text{Zn}$  centroid reaction rate.

$i$	$a_0$	$a_1$	$a_2$	$a_3$	$a_4$	$a_5$	$a_6$
1	$-2.70569 \times 10^{+1}$	$-2.54150 \times 10^{+0}$	$-4.59592 \times 10^{-4}$	$4.46992 \times 10^{-3}$	$-5.27022 \times 10^{-4}$	$2.68353 \times 10^{-5}$	$-1.50113$
2	$-1.09645 \times 10^{+1}$	$-3.81827 \times 10^{+0}$	$1.79997 \times 10^{-2}$	$-4.00723 \times 10^{-2}$	$5.02873 \times 10^{-3}$	$-4.19260 \times 10^{-4}$	$-1.48386$
3	$1.45160 \times 10^{+0}$	$-7.25300 \times 10^{+0}$	$-1.15250 \times 10^{-2}$	$4.54761 \times 10^{-2}$	$-3.78671 \times 10^{-3}$	$4.62772 \times 10^{-4}$	$-1.45082$
4	$6.17102 \times 10^{+0}$	$-1.15201 \times 10^{+1}$	$-1.08160 \times 10^{-2}$	$1.93951 \times 10^{-1}$	$-1.02466 \times 10^{-3}$	$3.29115 \times 10^{-2}$	$-1.54743$
5	$7.93110 \times 10^{+0}$	$-1.62517 \times 10^{+1}$	$1.03977 \times 10^{-1}$	$-6.19113 \times 10^{-2}$	$4.30871 \times 10^{-2}$	$-5.16600 \times 10^{-4}$	$-1.45643$
6	$7.11511 \times 10^{+0}$	$-1.54875 \times 10^{+1}$	$5.54672 \times 10^{-2}$	$-1.08431 \times 10^{-2}$	$1.08004 \times 10^{-2}$	$-7.96518 \times 10^{-4}$	$-1.41275$

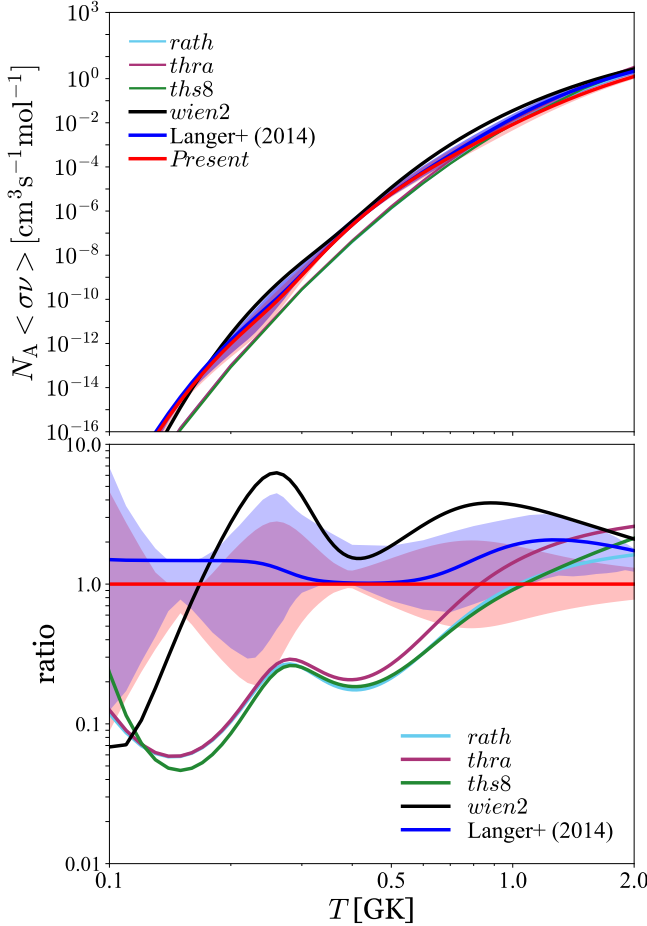


**Figure 4.** The comparison of  $^{57}\text{Cu}(p,\gamma)^{58}\text{Zn}$  thermonuclear reaction rates. Top Panel: the *rath*, *thra*, *ths8*, and *wien2* rates are the available rates compiled by Cyburt et al. (2010) and *wien2* is the recommended rate published in part of the JINA REACLIB v2.2 release. All available rates in JINA REACLIB v2.2 define  $S_p(^{58}\text{Zn})=2.277$  MeV. Bottom Panel: the comparison of the *Present* rate with Langer et al. rate and with the reaction rates compiled in the JINA REACLIB v2.2. The uncertainties of Langer et al. and the present rates are indicated as blue and red zones, respectively.

XRB models were used by Cyburt et al. (2016) and by Jacobs et al. (2018) to study the sensitivity of  $(\alpha,\gamma)$ ,  $(\alpha,p)$ ,  $(p,\gamma)$ , and  $(p,\alpha)$  nuclear reactions. The GS 1826–24 XRB models are continuously updated and were recently used by Goodwin et al. (2019) and by Johnston et al. (2020) to study the high density properties of accreted envelopes of GS 1826–24

clocked burster. The XRB models are fully self-consistent, which take into account of the correspondence between the evolution in astrophysical conditions and the feedback of nuclear energy generation in substrates of accreted envelope. Throughout an episode of outbursts, which may consist of a series of bursts with either an almost consistent or progressively increasing recurrence time, the models are capable to keep updating the evolution of chemical inertia and thermal configurations that drive the nucleosynthesis in the accreted envelope of an accreting neutron star.

The XRB models simulate a grid of Lagrangian zones (Weaver et al. 1978; Woosley et al. 2004; Heger et al. 2007), and each zone independently contains its own isotopic composition and thermal properties. We implement the time-dependent mixing length theory (Heger et al. 2000) to describe the convection transferring heat and nuclei between these Lagrangian zones. KEPLER uses an adaptive thermonuclear reaction network that automatically includes or discards the respective reactions out of the more than 6000 isotopes provided by JINA REACLIB v2.2 (Cyburt et al. 2010).

We adopt the XRB model from Jacobs et al. (2018) to compare with the observed burst light curves of the GS 1826–24 clocked burster. The model had been used by Jacobs et al. (2018) in a recent sensitivity study of nuclear reactions. To match the modeled light curve with the observed light curve and recurrence time,  $\Delta t_{\text{rec}}=5.14\pm 0.7$  h, of *Epoch Jun 1998* of GS 1826–24 burster, we adjust the accreted  $^1\text{H}$ ,  $^4\text{He}$ , and CNO metallicity fractions to 0.71, 0.2825, and 0.0075, respectively. The accretion rate is tuned to a factor of 0.122 of the Eddington-limited accretion rate,  $\dot{M}_{\text{Edd}}$ . This adjusted XRB model with the associated nuclear reaction library (JINA REACLIB v2.2) characterizes the *baseline* model in this work. Note that the *wien2* rate is the recommended  $^{57}\text{Cu}(p,\gamma)^{58}\text{Zn}$  reaction rate in JINA REACLIB v2.2. Other XRB models that adopt the same astrophysical configurations but implement the *Present*  $^{57}\text{Cu}(p,\gamma)^{58}\text{Zn}$ ; or the corrected  $^{55}\text{Ni}(p,\gamma)^{56}\text{Cu}$  (Valverde et al. 2019); or the *Present*  $^{57}\text{Cu}(p,\gamma)^{58}\text{Zn}$  and Valverde et al. corrected  $^{55}\text{Ni}(p,\gamma)^{56}\text{Cu}$ ; or the *Present*  $^{57}\text{Cu}(p,\gamma)^{58}\text{Zn}$ , Valverde et al. corrected  $^{55}\text{Ni}(p,\gamma)^{56}\text{Cu}$ , and Kahl et al.  $^{56}\text{Ni}(p,\gamma)^{57}\text{Cu}$  reaction rates are denoted as *Present*<sup>†</sup>, *Present*<sup>‡</sup>, *Present*<sup>♣</sup>, and *Present*<sup>§</sup> models, respectively. The *Present*<sup>§</sup> model implements a factor of 0.120 of  $\dot{M}_{\text{Edd}}$  for the accretion rate in order to obtain a modeled recurrence time close to the observation.

We then simulate a series of 40 consecutive XRBs for *baseline*, *Present*<sup>†</sup>, *Present*<sup>‡</sup>, *Present*<sup>♣</sup>, and *Present*<sup>§</sup> models; and only the last 30 bursts are summed up with respect

to the time resolution and then averaged to yield a burst light-curve profile. The first 10 bursts simulated from each model are excluded because these bursts undergo a transition from a chemically fresh envelope with unstable burning to an enriched envelope with chemically burned-in burst ashes and stable burning. Throughout the transition, the enriched burst ashes are recycled in the succeeding burst heating which gradually stabilize the following bursts. The averaging procedure applied on the modeled light curves is similar to the method performed by Galloway et al. (2017) to produce an averaged light-curve profile from the observed data set of *Epoch Jun 1998*. The epoch was recorded by the *Rossi X-ray Timing Explorer* (RXTE) Proportional Counter Array (Galloway et al. 2004, 2008, 2020) and were compiled into the Multi-Instrument Burst Archive<sup>4</sup> by Galloway et al. (2020).

The yielded burst luminosity,  $L_x$ , from each model is transformed and related to the observed flux,  $F_x$ , via the relation (Johnston et al. 2020),

$$F_x = \frac{L_x}{4\pi d^2 \xi_b (1+z)^2}, \quad (12)$$

where  $d$  is the distance;  $\xi_b$  takes into account of the possible deviation of the observed flux from an isotropic burster luminosity due to the scattering and blocking of the emitted electromagnetic wave by the accretion disc (Fujimoto et al. 1988; He et al. 2016); and the redshift,  $z$ , re-scales the light curve when transforming into an observer's frame. The  $d$  and  $\xi_b$  are combined to form the modified distance  $d\sqrt{\xi_b}$  by assuming that the anisotropy factors of burst and persistent emissions are degenerate with distance. We include the entire burst timespan of an averaged observational data to fit our modeled burst light curves of each model to the observed light curve. The best-fit  $d\sqrt{\xi_b}$  and  $(1+z)$  factors of the *baseline*, *Present<sup>†</sup>*, *Present<sup>‡</sup>*, *Present<sup>♣</sup>*, and *Present<sup>§</sup>* modeled light curves to the averaged-observed light curve and recurrence time of *Epoch Jun 1998* are 7.28 kpc and 1.29, 7.32 kpc and 1.29, 7.32 kpc and 1.29, 7.32 kpc and 1.28, 7.62 kpc and 1.29, respectively. Using these redshift factors, we obtain a set of modeled recurrence times which are close to the observation. The recurrence times of *baseline*, *Present<sup>†</sup>*, *Present<sup>‡</sup>*, *Present<sup>♣</sup>*, and *Present<sup>§</sup>*, are 4.85 h, 4.91 h, 4.91 h, 4.88 h, and 4.95 h, respectively. Though further reducing the accretion rate for each model improves the matching between modeled and observed recurrence time, all modeled burst light curves remain similar. For instance, the recurrence time of the *Present<sup>§</sup>* model  $\Delta t_{\text{rec}}=4.95$  h is produced with defining accretion rate as  $0.120 M_{\text{Edd}}$  and the produced burst light curve is similar to other modeled light curves in the present work.

The top panel of Fig. 5 illustrates the comparison between the best-fit modeled and observed XRB light curves. The evolution time of light curve is relative to the burst-peak time,  $t=0$  s. The overall averaged flux deviations between the

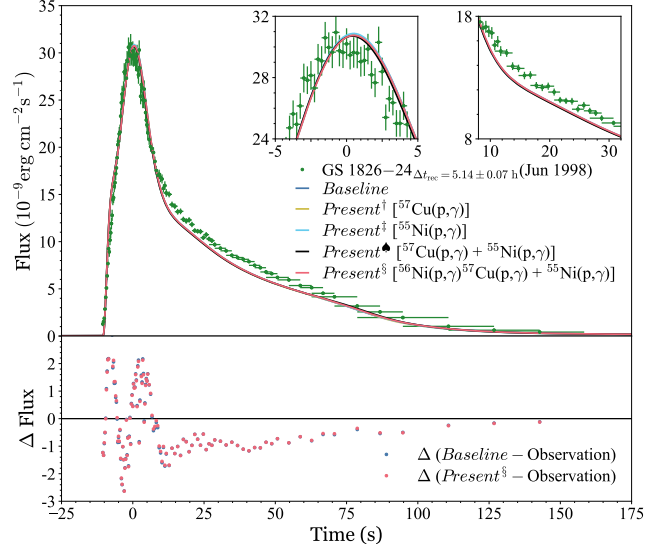


**Figure 5.** The light curves of GS 1826–24 clocked burster as a function of time. Top Panel: the best-fit *baseline*, *Present<sup>†</sup>*, *Present<sup>‡</sup>*, *Present<sup>♣</sup>*, and *Present<sup>§</sup>* modeled light curves to the observed light curve and recurrence time of *Epoch Jun 1998*. Both insets in the Top Panel magnify the light curve portions at  $t=-5$  to 5 s (left inset) and at  $t=8$  to 32 s (right inset). Bottom Panel: the deviation between the best-fit *baseline* (or *Present<sup>§</sup>*) modeled light curves and the observed light curve.

observed epoch and each of these theoretical models, *baseline*, *Present<sup>†</sup>*, *Present<sup>‡</sup>*, *Present<sup>♣</sup>*, and *Present<sup>§</sup>*, in units of  $10^{-9} \text{erg cm}^{-2} \text{s}^{-1}$  are 1.154, 1.170, 1.172, 1.133, and 1.147, respectively. The deviations between the *Present<sup>§</sup>* (and *baseline*) and observed light curve throughout the whole timespan of the observed light curve are displayed in the bottom panel of Fig. 5.

The observed burst peak is thought to be located in the time regime  $t=-2.5 - 2.5$  s (top left inset in Fig. 5), and at the vicinity of the modeled light-curve peaks of *baseline*, *Present<sup>†</sup>*, *Present<sup>‡</sup>*, *Present<sup>♣</sup>*, and *Present<sup>§</sup>*. The modeled light curves of *baseline*, *Present<sup>†</sup>*, *Present<sup>‡</sup>*, *Present<sup>♣</sup>*, and *Present<sup>§</sup>* at the near-burst-peak region  $t=-4.5 - 5.5$  s are almost indiscernible.

All modeled light curves are less enhanced than the observed light curve at  $t=8 - 80$  s, and the decrement is even augmented at around  $t=13$  s and 40 s, increasing the deviation between the modeled and observed light curves (Bottom Panel in Fig. 5). From the time regime at  $t=78$  s onward until the burst tail end, all modeled burst light curves are enhanced. Overall, all modeled light-curve profiles are similar and note that the observed burst tail is reproduced from  $t=78$  s onward until the burst tail end.

To investigate the microphysics behind the difference between both modeled burst light curves of the *baseline* and *Present<sup>§</sup>* models, we consider the 39<sup>th</sup> and the 41<sup>st</sup> burst for the *baseline* and *Present<sup>§</sup>* models, respectively. These bursts resemble the respective averaged light curve profile

<sup>4</sup> <https://burst.sci.monash.edu/minbar/>

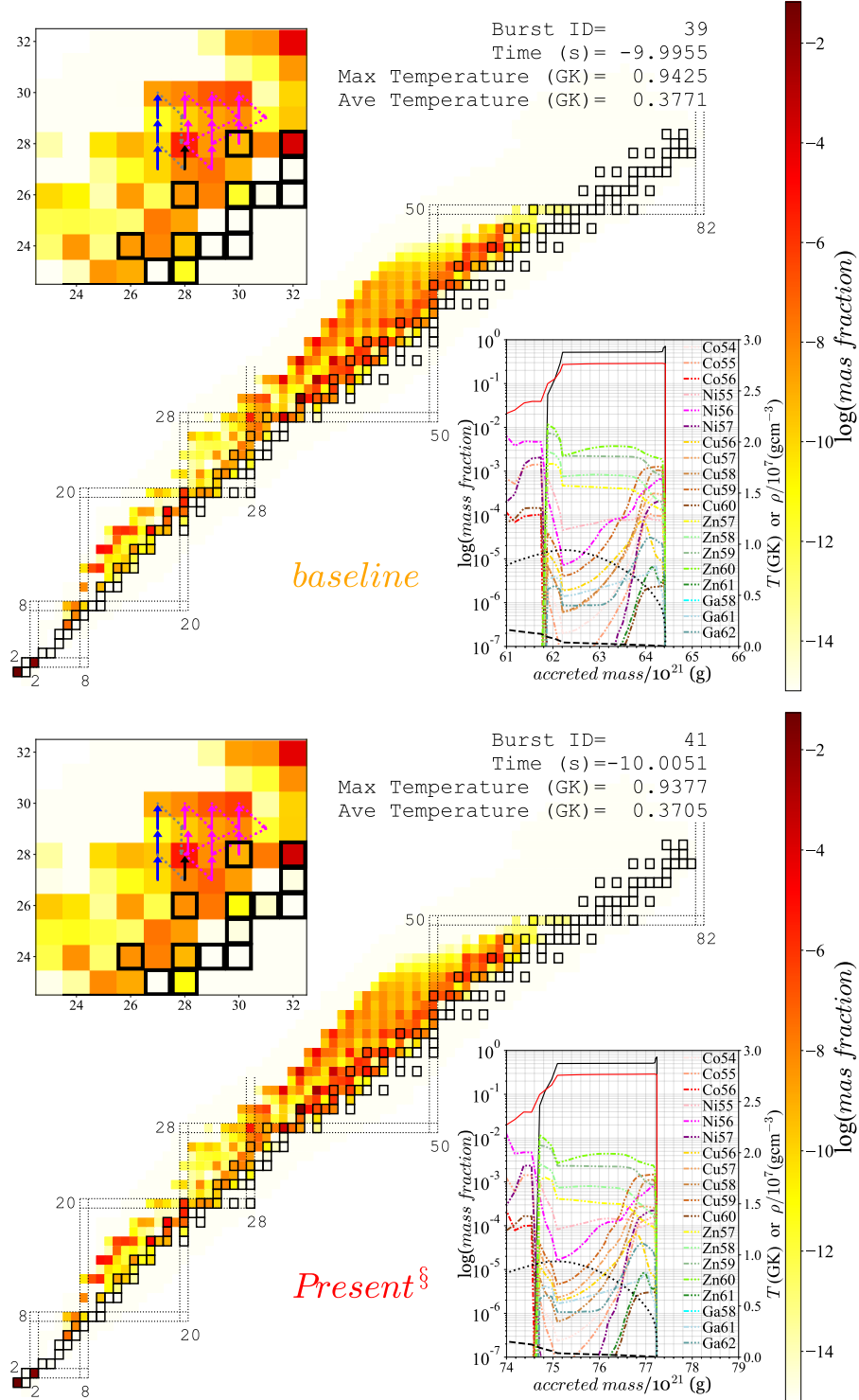


**Figure 6.** The nucleosynthesis and evolution of envelope corresponds to the moment just before the onset of the 39<sup>th</sup> burst for *baseline* (Top Panel) and of the 41<sup>st</sup> burst for *Present<sup>s</sup>* (Bottom Panel) scenarios. The averaged abundances of synthesized nuclei are represented by color tones referring to the right color scale in the nuclear chart of each panel. The black squares are stable nuclei. The top left insets in each panel magnify the regions related to the NiCu and ZnGa cycles. Pointing upward arrows indicate the  $(p,\gamma)$  reactions, whereas pointing downward arrows show the photodisintegration  $(\gamma,p)$  reactions. Slanting arrows from left to right depict  $(\beta^+\nu)$  decays and long slanting arrows from right to left represent  $(p,\alpha)$  reactions. These arrows are merely used to guide the eyes. The bottom right insets in each panel present the corresponding temperature (black dotted line) and density (black dashed line) of each mass zone, referring to right  $y$ -axis, and the abundances of synthesized nuclei, referring to left  $y$ -axis, in the accreted envelope regime where nuclei heavier than CNO isotopes are densely synthesized. The abundances of H and He are represented by black and red solid lines, respectively.

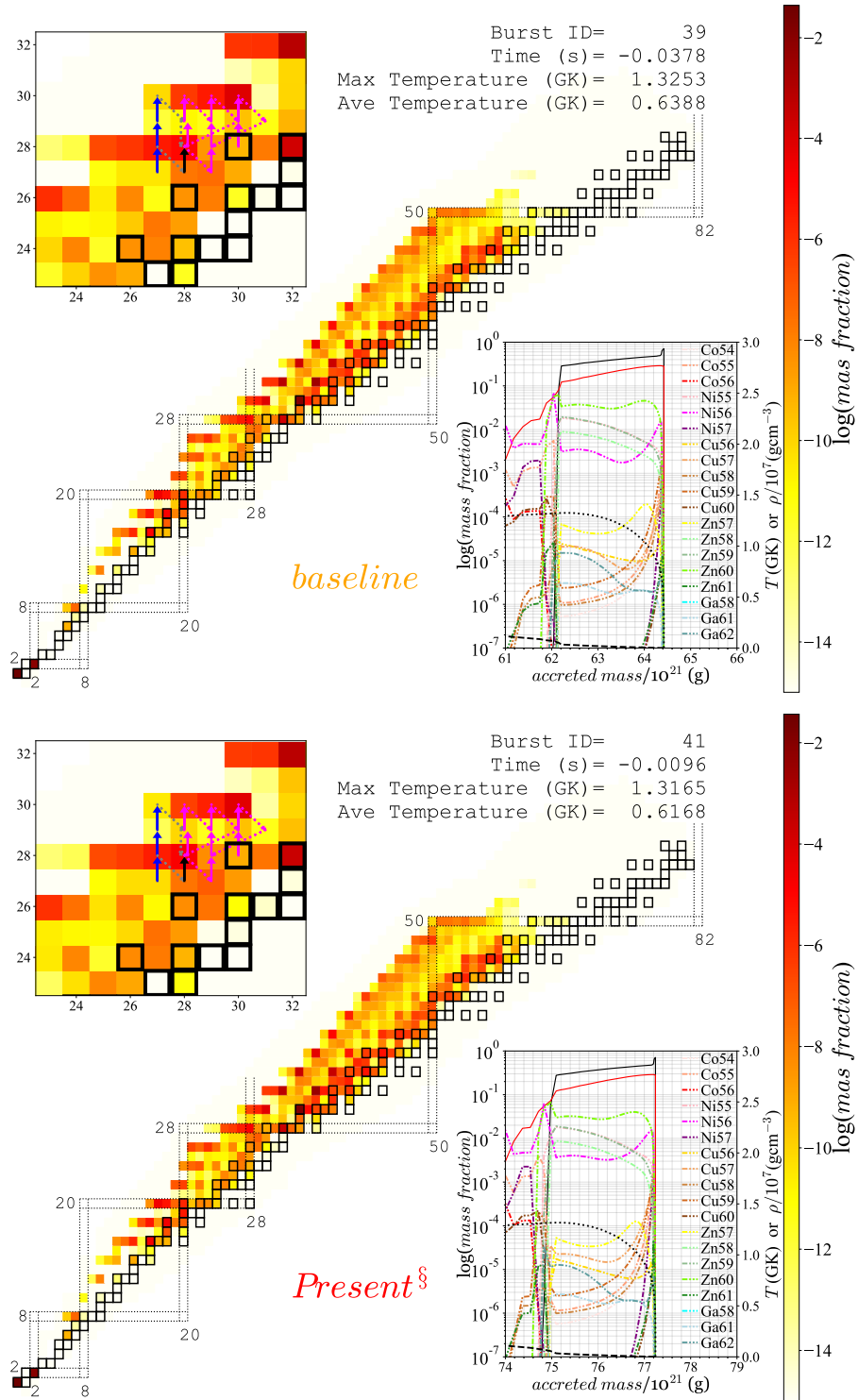


**Figure 7.** The nucleosynthesis and evolution of envelope corresponds to the moment at the immediate vicinity of the burst peak for *baseline* (Top Panel) and *Present<sup>§</sup>* (Bottom Panel) scenarios. See Fig. 6 for further description.



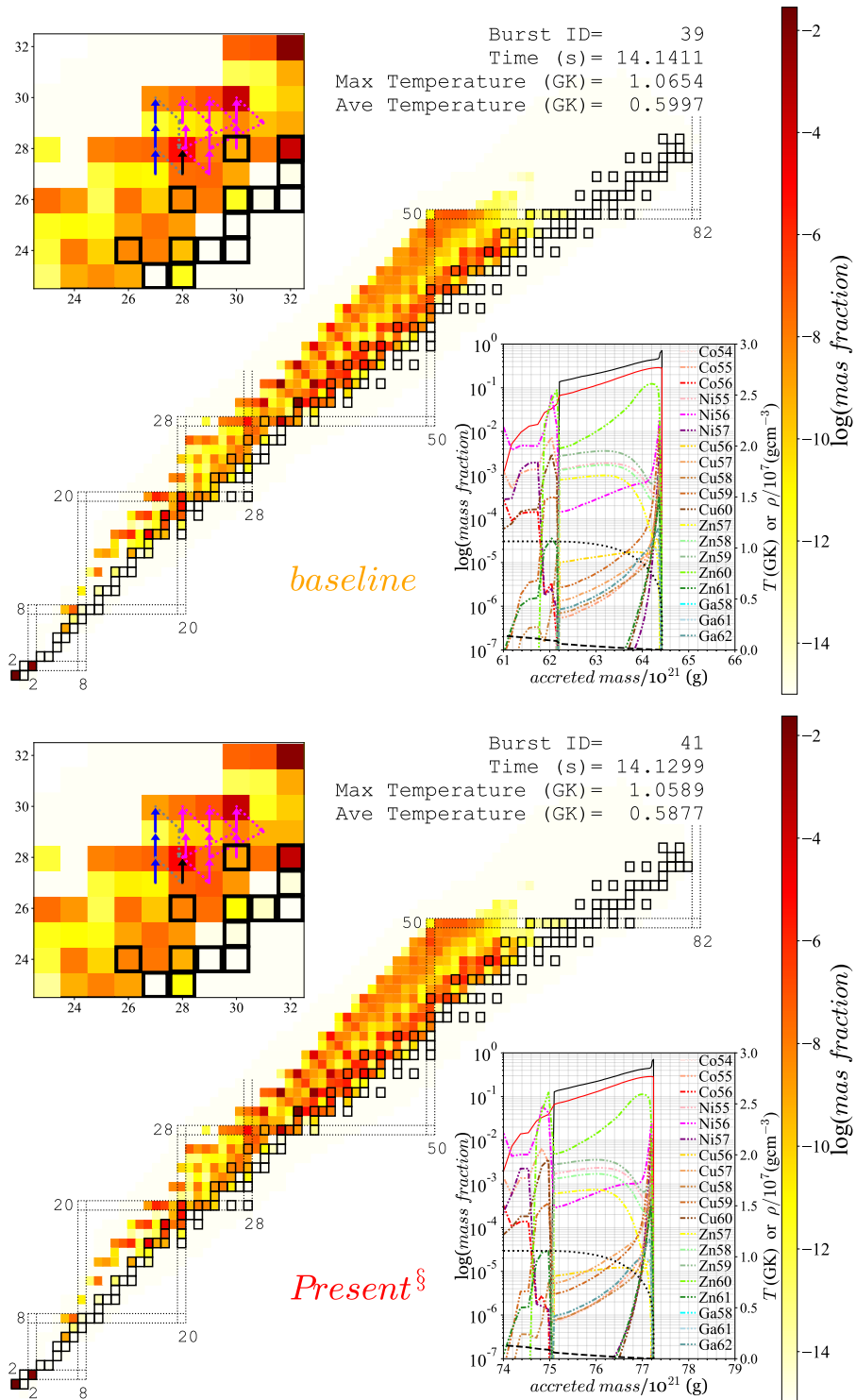


**Figure 8.** The nucleosynthesis and evolution of envelope corresponds to the moment of around 14 s after the burst peak for *baseline* (Top Panel) and *Present*<sup>§</sup> (Bottom Panel) scenarios. See Fig. 6 for further description.

presented in Fig. 5. The reference time of accreted envelope and nucleosynthesis in the following discussion is also relative to the burst-peak time,  $t=0$  s.

*The moment before and during the onset.*—After the preceding burst, the synthesized proton-rich nuclei in the accreted envelope go through  $\beta^+$  decays and enrich the region around stable nuclei with long half-lives, e.g.,  $^{60}\text{Ni}$ ,  $^{64}\text{Zn}$ ,  $^{68}\text{Ge}$ , and  $^{78}\text{Se}$ , which are the remnants of waiting points. When the accreted envelope evolves to the moment just before the onset of the succeeding XRB, due to the continuing nuclear reactions that occur in unburned hydrogen above the base of the accreted envelope, the temperature of the envelope increases up to a maximum value of 0.94 GK at the moment  $t=-10$  s for the *baseline* and *Present*<sup>§</sup> scenarios, see Fig. 6. At the moment just before the onset, some nuclei have already been synthesized and stored in the NiCu cycles, i.e. the NiCu I and II cycles (Van Wormer et al. 1994), and the sub-NiCu II cycle (Fig. 1), see the top left and bottom right insets in both panels of Fig. 6. Among the isotopes in the NiCu cycles, the highly synthesized nuclei having mass fractions of more than  $2 \times 10^{-4}$  are  $^{59}\text{Zn}$ ,  $^{58}\text{Zn}$ ,  $^{57}\text{Zn}$ ,  $^{58}\text{Ni}$ ,  $^{59}\text{Cu}$ ,  $^{58}\text{Cu}$ ,  $^{57}\text{Cu}$ ,  $^{60}\text{Cu}$  isotopes, and the  $^{56}\text{Ni}$  and  $^{60}\text{Zn}$  waiting points, whereas the  $^{56}\text{Co}$  and  $^{60}\text{Cu}$  isotopes having similar mass-fraction distributions in the envelope are converted to  $^{57}\text{Ni}$  and  $^{61}\text{Zn}$ , respectively (the lower right insets in both panels of Fig. 6).

We find that although the reaction flow induced by the  $^{55}\text{Ni}(p,\gamma)^{56}\text{Cu}(p,\gamma)^{57}\text{Zn}$  branch noticeably bypasses the  $^{56}\text{Ni}$  waiting point and enriches  $^{57}\text{Zn}$  for the *baseline* and *Present*<sup>§</sup> scenarios, it eventually has to go through the  $^{57}\text{Zn}(\beta^+\nu)^{57}\text{Cu}(p,\gamma)^{58}\text{Zn}$  branch and combines with the NiCu cycles and then breaks out from the NiCu cycles to the ZnGa cycles, see the upper left insets in both panels of Fig. 6. Due to the rather weak  $^{57}\text{Zn}(p,\gamma)^{58}\text{Ga}$  reaction, the  $^{55}\text{Ni}(p,\gamma)^{56}\text{Cu}(p,\gamma)^{57}\text{Zn}$  reactions and the subsequent  $^{57}\text{Zn}(\beta^+\nu)^{57}\text{Cu}(p,\gamma)^{58}\text{Zn}$  branch merely redirect an appreciable amount material away from the  $^{56}\text{Ni}$  waiting point, but the redirecting branch does not store material and not regulate the material flow. Moreover, the newly corrected  $^{55}\text{Ni}(p,\gamma)^{56}\text{Cu}$  reaction rate is lower than the one recommended in JINA REACLIB v2.2 (Fig. 2), causing less enrichment of  $^{57}\text{Zn}$  in the *Present*<sup>§</sup> scenario. This explains why neither the newly corrected nor the recommended  $^{55}\text{Ni}(p,\gamma)^{56}\text{Cu}$  reaction not exhibiting significant influence on the light curve of GS 1826–24 burster and abundances of synthesized heavier nuclei, and not as influential as claimed by Valverde et al. (2018, 2019). Note that the one-zone models used by Valverde et al. (2018, 2019) do not reproduce any burst light curves that are matched with observations. We remark that the *baseline* model that uses the recommended  $^{55}\text{Ni}(p,\gamma)^{56}\text{Cu}$  reaction rate in JINA REACLIB v2.2 has already manifested the possibility of the bypassing reaction flow of the  $^{56}\text{Ni}$  waiting point without replacing the recommended rate with Valverde et al. (2019) corrected rate because the recommended  $^{55}\text{Ni}(p,\gamma)^{56}\text{Cu}$  reaction rate is

stronger than the Valverde et al. corrected reaction rate, see Fig. 2.

The mass fraction of  $^{57}\text{Cu}$  in the *baseline* is lower than the one in the *Present*<sup>§</sup> scenario because the newly updated  $^{56}\text{Ni}(p,\gamma)^{57}\text{Cu}$  by Kahl et al. (2019) implemented in *Present*<sup>§</sup> is about up to a factor of 9 higher than the recommended  $^{56}\text{Ni}(p,\gamma)^{57}\text{Cu}$  rate from JINA REACLIB v2.2 used in *baseline* at temperature region around 1 GK. Nevertheless, the mass fraction of  $^{58}\text{Zn}$  in the *baseline* is slightly higher than the one in the *Present*<sup>§</sup> scenario. This reflects a stronger flow of  $^{57}\text{Cu}(p,\gamma)^{58}\text{Zn}$  in the *baseline* than in the *Present*<sup>§</sup> scenario. Such stronger flow is because the recommended *wien2*  $^{57}\text{Cu}(p,\gamma)^{58}\text{Zn}$  reaction rate from JINA REACLIB v2.2 used in *baseline* is about up to a factor of 4 higher than the *Present*  $^{57}\text{Cu}(p,\gamma)^{58}\text{Zn}$  reaction rates at temperature region around 1 GK. Hence, a weak (strong) flow of the  $^{56}\text{Ni}(p,\gamma)^{57}\text{Cu}$  in the *baseline* (*Present*<sup>§</sup>) coupled with a strong (weak) flow of the  $^{57}\text{Cu}(p,\gamma)^{58}\text{Zn}$  in the *baseline* (*Present*<sup>§</sup>) eventually yield a set of almost similar mass fractions of  $^{58}\text{Zn}$  along the mass zones in the accreted envelope during the onset for both scenarios. On the other hand, the synthesized nuclei heavier than  $^{68}\text{Se}$  for the *baseline* is almost as extensive as the *Present*<sup>§</sup> scenario, see the nuclear chart in Fig. 6. This indicates the reaction flow is regulated at the  $^{60}\text{Zn}$  waiting point by the  $^{59}\text{Cu}(p,\alpha)^{56}\text{Ni}$  reaction that competes with the  $^{59}\text{Cu}(p,\gamma)^{60}\text{Zn}$  reaction. Furthermore, after the reaction flow breaks out from the NiCu cycles through the  $^{59}\text{Cu}(p,\gamma)^{60}\text{Zn}(p,\gamma)^{61}\text{Ga}$  branch to the ZnGa cycles (Van Wormer et al. 1994), it is stored in the ZnGa cycles before surging through the nuclei heavier than  $^{68}\text{Se}$ . We find that the GeAs cycle that involves  $^{64}\text{Ge}(p,\gamma)^{65}\text{As}(p,\gamma)^{66}\text{Se}$  reactions could transiently and weakly exist in the mid of onset until the moment after burst peak, see the nucleosynthesis charts in Figs. 6, 7, and 8. As the GeAs cycle only weakly exist for a brief period, the ZnGa cycles become the important and preceding cycles before the extensive H-burning via (p, $\gamma$ ) reactions in the region heavier than  $^{68}\text{Se}$ . A new  $^{65}\text{As}(p,\gamma)^{66}\text{Se}$  reaction rate based on a more precise  $^{66}\text{Se}$  mass is desired to constrain the transient period, nonetheless, the fact that the transient existence of the weak GeAs cycle is not ruled out for the GS 1826–24 burster.

A stronger flow of  $^{56}\text{Ni}(p,\gamma)^{57}\text{Cu}$  and a weaker flow of  $^{57}\text{Cu}(p,\gamma)^{58}\text{Zn}$  in the *Present*<sup>§</sup> scenario slightly hinders the production of  $^{58}\text{Zn}$  and causes the abundance of synthesized  $^{57}\text{Cu}$  higher than the  $^{57}\text{Cu}$  fraction in *baseline*. In addition, the combined effect of  $^{56}\text{Ni}(p,\gamma)^{57}\text{Cu}(p,\gamma)^{58}\text{Zn}$  reactions enhances the NiCu II cycle, causing the abundance of  $^{57}\text{Ni}$  in *Present*<sup>§</sup> is higher than the one in *baseline*, see the lower right insets in both panels of Figs. 6 and 7. We notice that the balance between the  $^{56}\text{Ni}(p,\gamma)^{57}\text{Cu}$  and  $^{57}\text{Cu}(p,\gamma)^{58}\text{Zn}$  reactions just redistributes the reaction flow to the NiCu II cycle and then the reaction flow eventually joins with the NiCu I cycle and branches out to the ZnGa cycles at the  $^{60}\text{Zn}$  waiting point or follows the  $^{60}\text{Cu}(p,\gamma)^{61}\text{Zn}(p,\gamma)^{62}\text{Ga}$  reactions branches out to the ZnGa II cycle. Then, the joint reaction flow surges through the proton-rich region heavier than  $^{64}\text{Ge}$  where (p, $\gamma$ ) reactions actively burn hydrogen and intensify

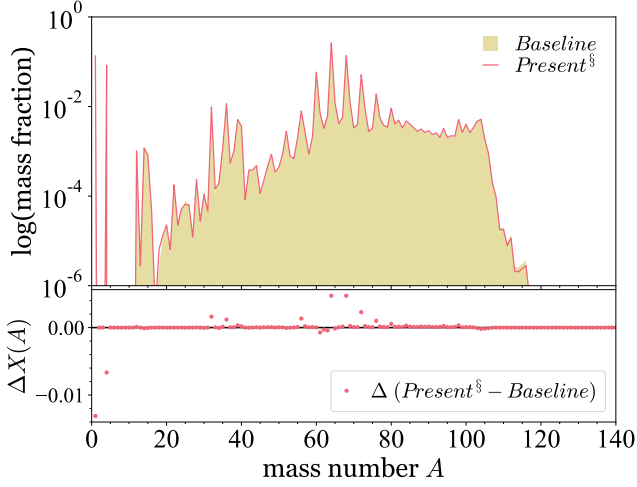


**Figure 9.** The averaged mass fractions for each mass number at burst tail when  $t=179.81^{+1.16}_{-1.16}$  s.

the rise of burst light curve from  $t=-10$  s up to  $t=0$  s (burst peak). As the redistributing and reassembling of reaction flow from the moment of onset until the burst peak yield a rather similar feature of abundances in the NiCu cycles (the lower right insets in both panels of Fig. 7), and the maximum envelope temperature of the *baseline* is slightly higher than the *Present<sup>s</sup>* scenario, these outcomes cause both burst peaks of the *baseline* and *Present<sup>s</sup>* scenarios almost close to each other, see the left inset in the upper panel of Fig. 5 and the maximum envelope temperatures in Fig. 7.

*The moment after the burst peak.* —At  $t=14.1$  s and  $T=1.06$  GK, the redistributing of reaction flow since the moment of onset mentioned above slightly keeps the reaction flow in NiCu cycles for somewhat longer time and slightly delays the reaction flow from passing through the waiting point  $^{60}\text{Zn}$  in the *Present<sup>s</sup>* scenario. The small delay allows the reaction flow to leak out from the NiCu cycles at later time and to burn hydrogen along the way reaching isotopes heavier than  $^{68}\text{Se}$  via  $(p,\gamma)$  reactions, and this situation mildly deviates the burst light curve of *Present<sup>s</sup>* from the light curve of *baseline*. Based on the analysis of the influence of  $^{57}\text{Cu}(p,\gamma)^{58}\text{Zn}$  reaction rate, we anticipate that if the actual energies of  $1_2^+$  and  $2_5^+$  resonance states are higher than the presently estimated ones using the IMME formalism, the contributions of these two resonance states to the total rate are exponentially reduced, and the  $2_4^+$  resonance state becomes the only dominant resonance at  $T=1-2$  GK for the  $^{57}\text{Cu}(p,\gamma)^{58}\text{Zn}$  reaction rate, and thus the modeled burst light curve is more diminished at the burst peak and at  $t=8-32$  s, whereas at  $t=65-150$  s, the *Present<sup>s</sup>* light curve is more enhanced compared to the *baseline* scenario.

The observed burst tail end of *Epoch Jun 1998* of GS 1826–24 burster is closely reproduced by the *baseline* and *Present<sup>s</sup>* models. The compositions of burst ashes generated by both models are presented in Fig. 9. The produc-

tions of nuclei  $A=60, 64,$  and  $68$  are affected in the *Present<sup>s</sup>* model. These nuclei mainly are the waiting points  $^{60}\text{Zn}, ^{64}\text{Ge}, ^{68}\text{Se}$ , and their daughter nuclei. These parent nuclei are the remnants from the ZnGa cycles, indicating that the ZnGa cycles are influenced by the NiCu cycles. The mass fractions of nuclei  $^{32}\text{S}, ^{36}\text{Ar}, ^{56}\text{Ni}$ , and decay products of  $^{72}\text{Kr}, ^{76}\text{Sr}$ , and  $^{80}\text{Zr}$  are also affected.

## 5. SUMMARY AND CONCLUSION

A theoretical study of  $^{57}\text{Cu}(p,\gamma)^{58}\text{Zn}$  reaction rate is performed based on the large-scale shell-model calculations in the full *pf*-model space using GXPF1a and its charge-dependent version, cdGX1A, interactions. We present a detailed analysis of the energy spectrum of  $^{58}\text{Zn}$  on the basis of the IMME concept with the aim to determine the order of  $1_1^+$  and  $2_3^+$  states of  $^{58}\text{Zn}$  that are dominant in the  $^{57}\text{Cu}(p,\gamma)^{58}\text{Zn}$  reaction rate at  $T=0.3-0.8$  GK. As no firm assignment can be done due to the lack of experimental information on  $^{58}\text{Cu}$  spectra, we test an alternative assignment to the previously adopted one. We have estimated the energy of  $1_2^+$  state of  $^{58}\text{Zn}$  based on the presently available candidate isobaric analogue states of  $^{58}\text{Cu}$  and  $^{58}\text{Ni}$ , which were experimentally determined, and the theoretical IMME  $c$  coefficient obtained from the isospin non-conserving interaction of *pf*-shell nuclei, cdGX1A. We estimate the  $1_2^+$  state of  $^{58}\text{Zn}$  to be higher than the one predicted by the isospin conserving interaction *pf*-shell interaction, GXPF1a. The dominance of the  $1_2^+$  state in the  $^{57}\text{Cu}(p,\gamma)^{58}\text{Zn}$  reaction rate at  $T=1-2$  GK is exponentially reduced.

Using the newly deduced  $^{57}\text{Cu}(p,\gamma)^{58}\text{Zn}$ , the newly corrected  $^{55}\text{Ni}(p,\gamma)^{56}\text{Cu}$ , and the updated  $^{56}\text{Ni}(p,\gamma)^{57}\text{Cu}$  reaction rates, we find that four combinations of these three reactions yield a set of light-curve profiles similar to the one generated by the *baseline* model based on the Forstner et al. (2001) and Fisker et al. (2001) reaction rates which are labeled as *wien2* and *nfis*, respectively, in JINA REACLIB v2.2. Nevertheless, the abundances of nuclei  $A=60, 64,$  and  $68$  between the *baseline* and *Present<sup>s</sup>* scenarios in the burst ashes are quantitatively different. These two effects are due to the redistributing and reassembling of reaction flows in the NiCu cycles that reduce the influence of the  $^{57}\text{Cu}(p,\gamma)^{58}\text{Zn}$  reaction on the burst light curve and affect the nucleosyntheses of  $^{57}\text{Cu}, ^{58}\text{Zn}$ , and some nuclei in the ZnGa cycles. We remark that the observed burst tail end of *Epoch Jun 1998* of GS 1826–24 burster is closely reproduced by the *Present<sup>s</sup>* and *baseline* models with the slightly adjusted astrophysical parameters.

Furthermore, we find that the redistributing and reassembling of reaction flows in the NiCu cycles also diminish the impact of  $^{55}\text{Ni}(p,\gamma)^{56}\text{Cu}$  reaction though this by-passing reaction partially diverts material from the  $^{56}\text{Ni}$  waiting point, the reaction flow eventually joins with the NiCu cycles and leaks out to the ZnGa cycles. Indeed, as indicated by the one-dimensional multi-zone hydrodynamic model matching with the GS 1826–24 clocked burster, implementing the *nfis*  $^{55}\text{Ni}(p,\gamma)^{56}\text{Cu}$  reaction rate has already manifested the by-passing reaction flow of the  $^{56}\text{Ni}$  waiting point without the

implementation of Valverde et al. (2019)  $^{55}\text{Ni}(p,\gamma)^{56}\text{Cu}$  reaction rate.

In addition, we notice that the GeAs cycle involving the  $^{64}\text{Ge}(p,\gamma)^{65}\text{As}(p,\gamma)^{66}\text{Se}$  reactions may exist shortly around the mid of onset until after the burst peak. The period of this transient existence may depend on the precise determination of the  $S_p(^{66}\text{Se})$  value.

We are very grateful to N. Shimizu for suggestions in tuning the KSHELL code at the PHYS.T3 (Institute of Physics) and QDR4 clusters (Academia Sinica Grid-computing Centre) of Academia Sinica, Taiwan, to B. Blank for implementing the IMME framework, to M. Smith for using the Computational Infrastructure for Nuclear Astrophysics, to B. A. Brown for using the NuShell@MSU code, and to J. J. He for fruitful discussion. This work was financially supported by the Strategic Priority Research Program of Chinese Academy of Sciences (CAS, Grant Nos. XDB34000000

and XDB34020204) and National Natural Science Foundation of China (No. 11775277). We are appreciative of the computing resource provided by the Institute of Physics (PHYS.T3 cluster) and the ASGC (Academia Sinica Grid-computing Center) Distributed Cloud resources (QDR4 cluster) of Academia Sinica, Taiwan. Part of the numerical calculations were performed at the Gansu Advanced Computing Center. YHL gratefully acknowledges the financial supports from the Chinese Academy of Sciences President's International Fellowship Initiative (No. 2019FYM0002) and appreciates the laptop (Dell M4800) partially sponsored by Pin-Kok Lam and Fong-Har Tang during the pandemic of Covid-19. A.H. is supported by the Australian Research Council Centre of Excellence for Gravitational Wave Discovery (OzGrav, No. CE170100004) and for All Sky Astrophysics in 3 Dimensions (ASTRO 3D, No. CE170100013). N.S. is supported by the IN2P3/CNRS, France, Master Project – “Exotic nuclei, fundamental interactions and astrophysics”.

## REFERENCES

- Angulo, C., Arnould, M., Rayet, M., et al. 1999, *NuPhA*, 656, 3
- Audi, G., Kondev, F. G., Wang, M., et al. 2017, *ChPhC*, 41, 030001
- Brown, B. A. (WSPOT code),  
<http://www.nsl.msu.edu/~brown/reaction-codes/home.html>
- Brown, B. A. & Rae, W. D. M. 2014, *NDS*, 120, 115
- Brussaard, P. J., Glaudemans, P. W. M. 1977, Shell model Applications in Nuclear Spectroscopy (North-Holland, Amsterdam)
- Cyburt, R. H., Amthor, A. M., Ferguson, R., et al. 2010, *ApJS*, 189, 240
- Cyburt, R. H., Amthor, A. M., Heger, A., et al. 2016, *ApJ*, 830, 55
- Fisker, J. L., Barnard, V., Görres, J., et al. 2001, *ADNDT*, 79, 241
- Forstner, O., Herndl, H., Oberhummer, H., et al. 2001, *PhRvC*, 64, 045801
- Fowler, W. A. & Hoyle, F. 1964, *ApJS*, 9, 201
- Fowler, W. A., Caughlan, G. R., Zimmerman, B. A. 1967, *ARA&A*, 5, 525
- Fu, C. Y., Zhang, Y. H., Wang, M., et al. 2020, *PhRvC*, 102, 054311
- Fujimoto, M. Y. 1988, *ApJ*, 324, 995
- Fujita, Y., Fujita, H., Adachi, T., et al. 2002, *EPJA*, 13, 411
- Fujita, H., Fujita, Y., Adachi, T., et al. 2007, *PhRvC*, 75, 034310
- Galloway, D. K., Cumming, A., Kuulkers, E., et al. 2004, *ApJ*, 601, 466
- Galloway, D. K., Muno, M. P., Hartman, J. M., et al. 2008, *ApJS*, 179, 360
- Galloway, D. K., Goodwin, A. J., Keek, L. 2017, *PASA*, 34, e019
- Galloway, D. K., in 't Zand, J. J. M., et al. 2020, *ApJS*, 249, 32
- Goodwin, A. J., Heger, A., Galloway, D. K. 2019, *ApJ*, 870, 64
- He, C.-C. & Keek, L. 2016, *ApJ*, 819, 47
- Heger, A., Langer, N., Woosley, S. E. 2000, *ApJ*, 528, 368
- Heger, A., Cumming, A., Galloway, D. K., et al. 2007, *ApJL*, 671, L141
- Herndl, H., Görres, J., Wiescher, M., et al. 1995, *PhRvC*, 52, 1078
- Honkanen, J., Kortelahti, M., Eskola, K., et al. 1981, *NuPhA*, 366, 109
- Honma, M., Otsuka, T., Brown, B. A., et al. 2004, *PhRvC*, 69, 034335
- Honma, M., Otsuka, T., Brown, B. A., et al. 2005, *EPJA*, 25(S01), 499
- Horoi, M., Stoica, S., Brown, B. A. 2007, *PhRvC*, 75, 034303
- Iliadis, C. 2007, Nuclear Physics of Stars (Wiley, Weinheim)
- Jacobs, A. M., Heger, A., et al. 2018, *Burst Environment, Reactions and Numerical Modelling Workshop* (BERN18), 11 – 15 Jun, Monash Prato Centre, Tuscany, Italy.
- Johansson, E. K., Rudolph, D., Ragnarsson, I., et al. 2009, *PhRvC*, 80, 014321
- Johnston, Z., Heger, A., Galloway, D. K. 2020, *MNRAS*, 494, 4576
- Jongsma, H., Silva, A. D., Bron, J., et al. 1972, *NuPhA*, 179, 554
- Joss, P. C. 1977, *Nature*, 270, 310
- Joss, P. C. 1978, *ApJL*, 225, L123
- Kahl, D., Woods, P. J., Poxon-Pearson, T., et al. 2019, *PhLB*, 797, 134803
- Keek, L. and Heger, A. 2011, *ApJ*, 743, 189
- Lam, Y. H., Smirnova, N. A., Caurier, E. 2013, *PhRvC*, 87, 054304
- Lam, Y. H., Blank, B., Smirnova, N. A., et al. 2013, *ADNDT*, 99, 680
- Lam, Y. H., He, J. J., Parikh, A., et al. 2016, *ApJ*, 818, 78
- Langer, C., Montes, F., Aprahamian, A., et al. 2014, *PhRvL*, 113, 032502
- Ma, S. -B., Zhang, L. -Y., Hu, J. 2019, *Nucl. Sci. Tech.*, 30, 141
- Makino, F. 1988, *IAUC*, No. 4653 (1988)



- Meisel, Z., Deibel, A., Keek, L., et al. 2018, *JPG*, 45, 093001
- Möller, P., Nix, J. R., Myers, W. D., et al. 1995, *ADNDT*, 59, 185
- Nesaraja, C. D., Geraedts, S. D., Singh, B. 2010, *NDS*, 111, 897
- Ormand, W. E. & Brown, B. A. 1989, *NuPhA*, 491, 1
- Ormand, W. E. & Brown, B. A. 1995, *PhRvC*, 52, 2455
- Ong, W.-J., Langer, C., Montes, F., et al. 2017, *PhRvC*, 95, 055806
- Pearson, J. M., Nayak, R. C., Goriely, S. 1996, *PhLB*, 387, 455
- Poves, A., Sánchez-Solano, J., Caurier, E., Nowacki, F. 2001, *NuPhA*, 694, 157
- Rauscher, T. & Thielemann, F. -K. 2000, *ADNDT*, 75, 1
- Richter, W. A., Brown, B. A., Signoracci, A., et al. 2011, *PhRvC*, 83, 065803
- Richter, W. A., Brown, B. A. 2012, *PhRvC*, 85, 045806
- Richter, W. A., Brown, B. A. 2013, *PhRvC*, 87, 065803
- Rolfs, C. E. & Rodney, W. S. 1988, *Cauldrons in the Cosmos* (Univ. of Chicago Press, Chicago)
- Rudolph, H., McGrath, R. L. 1973, *PhRvC*, 8, 247
- Rudolph, D., Baktash, C., Dobaczewski, J., et al. 1998, *PhRvL*, 80, 3018
- Rudolph, D., Fahlander, C., Algora, A., et al. 2000, *PhRvC*, 63, 021301
- Rudolph, D., Andreoiu, C., Fahlander, C., et al. 2002, *PhRvL*, 89, 022501
- Schatz, H., Aprahamian, A., Görres, J., et al. 1998, *PhR*, 294, 167
- Schatz, H., Aprahamian, A., Barnard, V., et al. 2001, *PhRvL*, 86, 3471
- Schatz, H., Bertulani, C. A., Brown, B. A., et al. 2005, *PhRvC*, 72, 065804
- Schatz, H., Ong, W.-J. 2017, *ApJ*, 844, 139
- Seth, K. K., Iversen, S., Kaletka, M., et al. 1986, *PhLB*, 173, 397
- Shimizu, N., Mizusaki, T., Utsuno, Y., et al. 2019, *CPC*, 244, 372
- Smirnova, N. A., Blank, B., Brown, B. A., et al. 2016, *PhRvC*, 93, 044305
- Smirnova, N. A., Blank, B., Brown, B. A., et al. 2017, *PhRvC*, 95, 054301
- Smith, M., Lingerfelt, E., Nesaraja, C., Smith, C. Computational Infrastructure for Nuclear Astrophysics (CINA), <http://nucastrodata.org/infrastructure.html>
- Steiner, A. W., Lattimer, J. M., Brown, E. F. 2010, *ApJ*, 722, 33
- Surbrook, J., MacCormick, M., Bollen, G., et al. 2019, *Hyperfine Interact.*, 240, 65
- Tanaka, Y. 1989, in: Hunt, J. & Battrick, B. (Eds.), *Proc. 23rd ESLAB Symposium on Two Topics in X-Ray Astronomy*, Bologna, Italy, 13 – 20 Sept. (SP-296; ESTEC, Noordwijk, The Netherlands: ESA) p. 3.
- Xu, X., Zhang, P., Shuai, P., et al. 2016, *PhRvL*, 117, 182503
- Valverde, A. A., Brodeur, M., Bollen, G., et al. 2018, *PhRvL*, 120, 032701
- Valverde, A. A., Brodeur, M., Bollen, G., et al. 2019, *PhRvL*, 123, 239905E
- Ubertini, P., Bazzano, A., Cocchi, M., et al. 1999, *ApJ*, 514, L27
- Van Wormer, L., Görres, J., Iliadis, C., et al. 1994, *ApJ*, 432, 326
- Wallace, R. K. & Woosley, S. E. 1981, *ApJS*, 45, 389
- Weaver, T. A., Zimmerman, G. B., Woosley, S. E. 1978, *ApJ*, 225, 1021
- Wiescher, M., Harms, V., Gorres, J., et al. 1987, *ApJ*, 316, 162
- Wigner, E. P. 1957, in: *Proc. Robert A. Welch Found. Conf.* 1, p. 67, reproduced in: D. Robson, J. D. Fox (Eds.), *Nuclear Analogue States*, in: *Benchmark Papers in Nuclear Physics*, vol. 1, John Wiley & Sons, 1976, p. 39.
- Woosley, S. E. & Taam, R. E. 1976, *Nature*, 263, 101
- Woosley, S. E. & Weaver, T. A. 1984, in: *High Energy Transients in Astrophysics*, AIP Conf. Proc., Woosley S. E. (Ed), vol. 115, p. 273, AIP, New York
- Woosley, S. E., Heger, A., Cumming, A., et al. 2004, *ApJS*, 151, 75
- Zhang, Y. H., Zhang, P., Zhou, X. H., et al. 2018, *PhRvC*, 98, 014319